Nature. Author manuscript; available in PMC 2017 February 21.

Published in final edited form as:

Nature. 2016 June 23; 534(7608): 562–565. doi:10.1038/nature18595.

MOLECULAR ARCHITECTURE OF THE HUMAN SPERM IZUMO1 AND EGG JUNO FERTILIZATION COMPLEX

Halil Aydin[1], **Azmiri Sultana**[1], **Sheng Li**[2], **Annoj Thavalingam**[1], and **Jeffrey E. Lee**[1]

[1]Department of Laboratory Medicine and Pathobiology, Faculty of Medicine, University of Toronto, Toronto, ON M5S 1A8, Canada

[2]Department of Medicine, University of California, San Diego, La Jolla, CA 92093, USA

Abstract

Fertilization is an essential biological process in sexual reproduction and comprises a series of molecular interactions between the sperm and egg[1,2]. The fusion of haploid spermatozoon and oocyte is the culminating event in mammalian fertilization, enabling the creation of a new genetically distinct diploid organism[3,4]. The merger of two gametes is achieved through a two-step mechanism where the sperm Izumo1 on the equatorial segment of the acrosome-reacted sperm recognizes its receptor Juno, on the egg surface[4–6]. This is followed by the fusion of two plasma membranes. Izumo1 and Juno proteins are indispensable for fertilization as constitutive knockout of either Izumo1 or Juno result in mice that are healthy but infertile[5,6]. Despite their central importance in reproductive medicine, the molecular architectures and the details of their functional roles in fertilization are not known. Here, we present the crystal structures of the human Izumo1 and Juno in unbound and bound conformations. The human Izumo1 structure exhibits a distinct boomerang shape and provides the first structural insights into the Izumo family of proteins[7]. Human Izumo1 forms a high-affinity complex with Juno and undergoes a major conformational change within its N-terminal domain upon binding to the egg-surface receptor. Our results provide new insights into the molecular basis of sperm-egg recognition, cross-species fertilization, and barrier to polyspermy, thus promising benefits for the rational development of novel non-hormonal contraceptives and fertility treatments for humans and other species of mammals.

Correspondence and request for materials should be addressed to J.E.L. (jeff.lee@utoronto.ca).

Supplementary Information is linked to the online version of the paper at www.nature.com/nature

AUTHOR CONTRIBUTIONS

H.A. designed the project, performed all the cloning, mutagenesis, expression, purification, biophysical characterization and crystallization experiments, collected synchrotron X-ray diffraction data, and determined the crystal structures and SAXS reconstructions. A.S. assisted with BLI and SPR experiments and provided crystallographic guidance for refinement and validation of the crystal structures. A.T. assisted with protein expression and purification. H.A. prepared the samples and S.L. performed and analyzed the DXMS data. J.E.L supervised the research and assisted with BLI experiments. H.A. and J.E.L. analyzed, discussed all results, and wrote the manuscript.

AUTHOR INFORMATION

Atomic coordinates and structure factors have been deposited in the Protein Data Bank under accession codes: 5F4E ($Izumo1_{22-254}$-$Juno_{20-228}$ complex); 5F4Q ($Juno_{20-228}$); 5F4T ($Izumo1_{22-254}$); 5F4V ($Izumo1_{22-268}$) The authors declare no competing financial interests.

The journey of human sperm to an egg ends in the female oviduct, when the active sperm penetrates through the egg zona pellucida glycoprotein layer to reach the perivitelline space between the zona layer and the plasma membrane of the oocyte[8–10]. The active sperm then fuses with the oocyte membrane to allow the formation of the zygote[1,4]. At least two membrane-bound proteins, sperm Izumo1 and egg Juno, are essential in gamete recognition and/or the fusion process[5,6]. Both *izumo1* and *juno* genes are conserved in other mammals (Extended Data Fig. 1 and 2)[6,11].

Structural and biochemical studies of Izumo1 are hampered by difficulties in recombinant protein expression[12]. Using *Drosophila melanogaster* S2 cells, we expressed and purified the extracellular region of human Izumo1 (residues 22-254) by Ni^{2+}-affinity and gel filtration chromatography. Biophysical characterization of Izumo1 revealed a stable and monomeric protein with extensive mixed α/β secondary structural character (Extended Data Fig. 3). We obtained crystals of unbound $Izumo1_{22-254}$ and determined the structure at 3.1-Å resolution. $Izumo1_{22-254}$ is a monomer and adopts a distinct boomerang shape with dimensions of ~85-Å × 25-Å × 22-Å. The overall structure consists of two domains: a rod-shaped N-terminal four-helix bundle (4HB; residues 22-134) and a C-terminal immunoglobulin-like (Ig-like; residues 167-254) domain (Fig. 1 and Supplementary Fig. 1). Two anti-parallel β-strands (β1 and β2) function like a hinge between the 4HB and Ig-like domains.

The four helices in the Izumo1 4HB domain (h1, h2, h3 and h4) vary from 14 to 30 residues in length. The helices have amphipathic character with a polar surface exposed to solvent and hydrophobic residues packing into a core. The helices h1–h2 and h3–h4 are connected with short 5-residue loops (L1 and L3), while a longer 15-residue loop (L2) links h2 to h3. The 4HB and hinge regions are stabilized by an extensive network of disulphide linkages (C22–C149, C25–C152, C135–C159, C139–C165) and charge-charge interactions (H44-D101, E80-K154, and R96-E110) that are conserved in almost all Izumo1 orthologs and other Izumo family proteins (Extended Data Fig. 1 and Supplementary Fig. 2).

The $Izumo1_{22-254}$ Ig-like domain resides at the membrane-proximal end of the molecule. It adopts a seven-stranded (A, B, C, C′, E, F, G) β-sandwich with the two β-sheets covalently linked with an Ig-superfamily (IgSF) conserved disulphide bond (C182–C233) between strands B and F (Fig. 1). Seven-stranded Ig-like folds classically consist of a 3+4 arrangement with β-strands A, B and E forming β-sheet 1, and β-strands C, C′, F and G forming β-sheet 2[13] (Supplementary Fig. 3). The $Izumo1_{22-254}$ Ig-like domain has a novel 2+5 organization representing a new IgSF subtype. In $Izumo1_{22-254}$, strand A interacts with β-sheet 2 rather than β-sheet 1. The disulphide bond preceding β-strand A (C139–C165) may constrain the movement of the strand toward β-sheet 1 resulting in this strand switch (Supplementary Fig. 3). We also determined the crystal structure of a slightly longer $Izumo1_{22-268}$ construct at 2.9-Å resolution to gain insights into the C-terminal linker region immediately following the Ig-like domain. The $Izumo1_{22-268}$ structure superimposes well with $Izumo1_{22-254}$ (rmsd 1.0-Å over all atoms) (Supplementary Fig. 4). However, no electron density was observed after residue 256, suggesting that the linker region following the Ig-like domain is flexible.

Juno (previously known as folate receptor-δ (FOLR-δ)) is a glycophosphatidylinositol (GPI)-anchored, cysteine-rich glycoprotein displayed on the egg surface that was demonstrated to be the egg receptor of Izumo1[6]. We determined the crystal structure of the unbound $Juno_{20-228}$ at 1.8-Å resolution. $Juno_{20-228}$ has a globular architecture that is composed of five short α–helices (h1, h2, h3, h4 and h5), three 3_{10} helices and two short two-stranded antiparallel β-sheets (Fig. 1 and Supplementary Fig. 1). Eight conserved disulphide bonds stabilize the core helices h1, h2, h3 and h4, and flexible loops. Juno shares sequence and structural similarity to the human FOLR-α and FOLR-β (~58% sequence identity and ~1-Å rmsd over 197 Cα atoms)[14,15] (Extended Data Fig. 4). Despite the close similarities, six key folate binding residues in FOLR-α and FOLR-β are not conserved in human Juno, thus supporting previous observations that Juno does not bind folate[6,14,15] (Extended Data Fig. 4). While this manuscript was under revision, a partial structure of murine Juno was determined (Supplementary Fig. 5)[16].

Biolayer interferometry (BLI) and surface plasmon resonance (SPR) was used to measure the binding affinities of human Izumo1 and Juno. The interaction is stable with a dissociation constant (K_d) between ~48–60 nM (Extended Data Fig. 3). In addition, $Izumo1_{22-254}$ and $Juno_{20-228}$ co-purify as a 1:1 complex on size exclusion chromatography. Our results indicate that these two proteins instead engage in a stable complex during the gamete fusion process. To understand the precise molecular interactions of Izumo1-Juno, we determined the structure of $Izumo1_{22-254}$-$Juno_{20-228}$ complex at 2.4-Å resolution. In the asymmetric unit, we observed one $Izumo1_{22-254}$ molecule binding to one $Juno_{20-228}$ molecule with an interface that spans over ~910 $Å^2$ surface area (Fig. 2 and Extended Data Fig. 5). Izumo1 has been shown to interact with Juno via its N-terminal domain[17]. The crystal structure indicates that residues from all three Izumo1 regions (4HB, hinge and Ig-like) contact $Juno_{20-228}$ through extensive non-bonded van der Waals, hydrophobic and aromatic interactions (>60% of total interface interactions) (Extended Data Fig. 5). There are also two intermolecular salt bridges ($K163_{Juno}$-$E71_{Izumo1}$ and $E45_{Juno}$-$R160_{Izumo1}$) and eight hydrogen bond interactions at the interface (Fig. 2 and Extended Data Fig. 5). However, all of these interactions are >3.0-Å apart, suggesting these are weak in nature.

Structural comparison of $Izumo1_{22-254}$ and $Juno_{20-228}$ alone to their bound states revealed no major structural differences in $Juno_{20-228}$ or the Ig-like domain of Izumo1 upon complex formation (Fig. 3). A major conformational change was observed in the 4HB and hinge regions. All four helices in the 4HB move ~20-Å towards $Juno_{20-228}$, whereas the L2 and hinge regions shift ~8-Å upon binding. As a result, the bound $Izumo1_{22-254}$ abandons its distinct boomerang shape and adopts an upright conformation. The structural constraints from the short loops between the h1–h2 and h3–h4 helices allow the 4HB domain to translate as a single unit (Fig. 3).

In order to understand the conformational dynamics of the Izumo1-Juno interaction in solution, we utilized a hybrid approach that combined small angle X-ray scattering (SAXS) and deuterium exchange mass spectrometry (DXMS). *Ab initio* SAXS reconstructions of unbound $Izumo1_{22-254}$ revealed a distinct boomerang shape, similar to its crystal structure (Extended Data Fig. 6). Upon $Juno_{20-228}$ binding, $Izumo1_{22-254}$ adopts an upright conformation. Our DXMS studies revealed that the residues lining at the binding interface

exhibited a reduced exchange profile in the complex compared to the unbound states (Fig. 4, Extended Data Fig. 6 and Supplementary Fig. 6). Moreover, DXMS experiments performed on Izumo1 alone indicated a high level of exchange in the hinge region, thus suggesting dynamic flexible motion within this region. Upon Juno binding, deuterium exchange of residues 127-140 in the hinge region was reduced by >50%, which is more than the reduction seen by residues at the Izumo1-Juno interface (Fig. 4). The strong level of H/D protection is due to the formation of 10 additional main chain hydrogen bonds within residues 127-140 of the hinge region. This suggests that the Izumo1 hinge region is stabilized in a "locked" upright position in the presence of Juno.

Mutational studies at the Izumo1-Juno interface revealed the structural determinants required for binding (Fig. 2, Extended Data Table 1 and Supplementary Fig. 7). Upon binding to $Juno_{20\text{-}228}$, a D72-Q130 hydrogen bond found between Izumo1 L2 and the 4HB α4 helix is disrupted to form a new intermolecular salt bridge ($E71_{Izumo1}$-$K163_{Juno}$) at the interface (Fig. 3). Alanine mutations to Izumo1 D72 and Q130 did not affect binding to Juno, as these residues are not involved at the interface. Alanine and charge reversal mutations to the intermolecular $E71_{Izumo1}$-$K163_{Juno}$ salt bridge reduced the K_d ~2-fold, suggesting this ion pair plays a minor role in binding. Mutations to the $R160_{Izumo1}$-$E45_{Juno}$ intermolecular salt bridge result in ~50-fold reduction in binding affinities, suggesting a major role for this second electrostatic interaction in Izumo1-Juno recognition. Using SAXS, we characterized the binding mode of Izumo1 and Juno salt bridge mutants that hindered high affinity complex formation. The SAXS scattering data and reconstructions show no major change compare to the wild-type Izumo1-Juno complex, and suggest proper complex formation despite up to 50-fold decrease in affinity (Extended Data Fig. 7). Significant reductions in binding (>20-fold) were also observed with mutations to Izumo1 and Juno residues that are conserved in most mammals ($W148_{Izumo1}$, $H157_{Izumo1}$, $W62_{Juno}$ and $L81_{Juno}$). In fact, an alanine mutation to $W148_{Izumo1}$ completely abolished Izumo1-Juno binding. These results are in excellent agreement with the cell-oocyte binding assay presented in an accompanying crystal structure of the same complex[18]. Taken together, our mutagenesis study suggests that the interface is likely stabilized through the combined effects of multiple van der Waals, hydrophobic, aromatic and electrostatic interactions. This allows the Izumo1-Juno interface to be resilient to mutations.

Although we observed discernible sequence conservation at the complex interface in both proteins, comparative sequence analysis revealed significant variations among a number of interface residues. Approximately one-half of the residues (Juno: Y44, E45, L58, F77, M83, R87, M145, Y147, K163 and Izumo1: L69, V141, K150, N151, K153, E155, A158, Y163, N239, S241) vary across mammalian species (Extended Data Fig. 1 and 2). Similar to the species-specific recognition employed by glycoproteins in the zona pellucida that surrounds the egg, these residues may act to restrict a productive Izumo1 and Juno binding event to a specific pair of species[9,19,20]. For example, in primates, these residues are mainly preserved (Extended Data Fig. 1 and 2), suggesting that the species-specific diversification of Izumo1 and Juno may be restricted to non-primate mammals.

Our structural characterizations indicate that the human Izumo1 does not have properties predictive of viral, intracellular and developmental fusogens, such as influenza A virus

hemagglutinin (HA) and *C. elegans* epithelial fusion failure-1 (EFF-1) proteins[21–23] (Extended Data Fig. 8). This suggests that Izumo1 does not seem to function as a direct fusion protein. At least three different fusion mechanisms are possible (Extended Data Fig. 9). Firstly, Izumo1 may act as a scaffold to recruit a protein complex that contains or regulates other fusion proteins. The requirement of a multiprotein complex for fusion is not unusual, as some viruses, such as herpes simplex virus-1 or Epstein Barr virus requires the formation of a multicomponent fusion complex[24,25]. Alternatively, Inoue *et al.* proposed that monomeric Izumo1 on the sperm surface interacts with Juno[26]. Subsequently, a protein disulphide isomerase facilitates the dimerization of Izumo1 to allow an interaction with another oocyte receptor to facilitate fusion. Finally, the tight heterotypic interaction between human Izumo1 and Juno proteins may be sufficient to bring close apposition of the sperm and egg membranes leading to fusion. Regardless, the conformational changes within Izumo1 suggest that receptor adhesion triggers the progression of the 4HB domain to the vicinity of the egg membrane and the conformational switch may be part of the structural changes required for fusion. After fusion, the fertilized egg rapidly sheds Juno molecules into the perivitelline space[6]. Given our measured tight nanomolar affinities between Izumo1 and Juno, shed Juno may essentially act as a rapid “sperm-sink” to neutralize incoming acrosome-reacted sperm as an additional polyspermy block. This process may be analogous to the shedding of viral glycoproteins (e.g. Ebola virus shed and soluble GP), which are able to act as a decoy to absorb antibody responses[27,28].

METHODS

Protein expression and purification

The genes corresponding to full-length human Izumo1 (GenBank accession number: NM_182575, residues 1-350) and human Juno (GenBank accession number: NM_001199206, residues 1-250) were codon optimized for expression in *Drosophila melanogaster* and gene synthesized (Integrated DNA Technologies). The DNA sequences encoding the extracellular regions of Izumo1 (residues 22-254 and 22-268) and Juno (residues 20-228) with a BiP signal peptide were subcloned into a modified pMT-puromycin expression vector (Invitrogen). All protein constructs contain a thrombin cleavage site and 10X-His affinity tag at the C-terminus. Binding interface mutants of $Izumo1_{22\text{-}254}$ and $Juno_{20\text{-}228}$ were generated using a modified QuikChange PCR-based site-directed mutagenesis protocol. The resulting wild-type and mutant $Izumo1_{22\text{-}254}$, $Izumo1_{22\text{-}268}$ and $Juno_{20\text{-}228}$ pMT expression plasmids were stably transfected in Drosophila S2 cells (Invitrogen) using Effectene transfection reagent (Qiagen), according to manufacturer’s protocol. Briefly, Drosophila S2 cells were cultured in Schneider’s medium (Lonza) supplemented with 10% (v/v) heat-inactivated fetal bovine serum (FBS) plus 1X antibiotic-antimycotic (Gibco), and propagated at 27°C. The day before transfection, 3×10^6 cells were seeded per well in a 6-well plate (Corning) with 3.0 ml complete growth medium and incubated overnight. On the day of transfection, 2 μg expression plasmid was mixed with the transfection reagents and the transfection complexes were added drop-wise onto the S2 cells. At 72 hours post-transfection, the cultured media were replaced with fresh S2 growth media supplemented with 6 μg ml^{-1} puromycin (Bioshop). Subsequently, S2 cells were gradually adapted to FBS-free Insect-XPRESS growth media (Lonza) with 6 μg ml^{-1} puromycin.

Stably transfected cells were grown to 1×10^7 cells ml^{-1} in Insect-XPRESS growth media using vented 2 L polycarbonate Erlenmeyer flasks (VWR) at 27°C. Protein expression was induced with 500 μM final concentration of sterile-filtered $CuSO_4$. Cultured media were harvested 6-days post-induction, clarified by centrifugation at 6750x*g* for 20 minutes, concentrated and buffer exchanged into Ni-NTA binding buffer (20 mM Tris-HCl [pH 8.0], 300 mM NaCl, 20 mM imidazole) using a Centramate tangential flow filtration system (Pall Corp.) All Izumo1 and Juno proteins were purified by Ni-NTA metal affinity chromatography. Eluted samples were buffer exchanged into TBS (10 mM Tris-HCl [pH 8.0], 150 mM NaCl) using a PD-10 desalting column (GE Life Sciences) and thrombin (EMD Millipore) digested at 22°C for 24 hours (1:2000 (w/w) enzyme to protein ratio). The cleaved protein samples were then buffer exchanged to a low pH buffer (10 mM sodium acetate [pH 5.6], 150 mM NaCl) and enzymatically deglycosylated using 100 units Endoglycosidase H (New England Biolabs) per mg of Izumo1 or Juno at 22°C for 16 hours. To prepare the Izumo1-Juno protein complexes, deglycosylated $Izumo1_{22\text{-}254}$ and $Juno_{20\text{-}228}$ samples were mixed at a molar ratio of 1:1 and incubated at 22°C for 2 hours prior to size exclusion chromatography on a custom prep-grade Superdex-200 XK 16/70 column equilibrated with TBS. Peak fractions were pooled and protein concentrations were quantified by measuring A_{280}.

Circular dichroism (CD) spectroscopy

CD spectra of human $Izumo1_{22\text{-}268}$ were acquired on a Jasco J-810 spectropolarimeter using a 1 mm quartz cuvette (Helma). CD measurements were conducted with 50 to 100 μM protein sample purified in 10 mM potassium phosphate [pH 7.5] and 150 mM NaCl buffer. Wavelength scans were recorded at 25°C between 190 nm and 250 nm and averaged over 5 accumulations. Data were converted to mean residue ellipticity and secondary structure content was estimated using the K2D algorithm within the DichroWeb analysis server[29]. Thermal denaturation assays were performed at a wavelength of 222 nm by increasing the temperature from 20°C to 99°C and monitoring the change in ellipticity as a function of temperature. The data were baseline corrected with buffer blank, normalized between 0 (folded) and 1 (unfolded) and fit to a nonlinear biphasic sigmoidal curve using GraphPad Prism (GraphPad Software, San Diego, CA USA).

Dynamic light scattering (DLS)

$Izumo1_{22\text{-}254}$, $Juno_{20\text{-}228}$, and $Izumo1_{22\text{-}254}$-$Juno_{20\text{-}228}$ complex samples were prepared in TBS with 2% (v/v) glycerol and concentrated to 0.5, 1.0, 1.5, 2.0, 2.5, 3.0, 4.0 and 5.0 mg ml^{-1} prior to the DLS measurements. DLS experiments were performed at 25°C on a DynaPro Plate Reader II (Wyatt Technology). For each condition, 22 μl of sample was loaded in triplicate onto a black 384-well clear-bottom plate (Greiner). Data acquisition was recorded over 5 seconds with a total of 10 acquisitions for each concentration. The polydispersity and hydrodynamic radius (R_H) of the molecules in solution was calculated using the Dynamics (v.7) software (Wyatt Technology).

Size Exclusion Chromatography-Multiangle Light Scattering (SEC–MALS)

The oligomeric state of tag-removed, glycosylated $Izumo1_{22\text{-}268}$ was assessed by multiangle light scattering. Monomeric bovine serum albumin (BSA) standard (2 mg ml^{-1}; M_w =

66,432 Da) dissolved in PBS buffer (10 mM Phosphate [pH 7.4], 2.7 mM KCl, 137 mM NaCl) was used to calibrate the MALS detectors. Izumo1$_{22-268}$ was first purified on an analytical Superdex-75 10/300 GL size exclusion column equilibrated in PBS buffer to ensure proper monodispersity. Then, 600 μg of Izumo1$_{22-268}$ was applied onto a PBS-equilibrated Superdex-200 Increase 10/300 GL size exclusion column in-line with a Viscotek MALS detector (Malvern). The data were processed and weight-averaged molecular mass was calculated using the OMNISEC (v. 5.1) software package (Malvern).

Biolayer interferometry (BLI)

The binding affinities of Izumo1$_{22-254}$ to Juno$_{20-228}$ was measured by biolayer interferometry using a single-channel BLItz instrument (Pall FortéBio), based on protocols previously described[30]. Briefly, purified wild-type or mutant Juno$_{20-228}$ in PBS buffer was biotinylated using the EZ link sulfo-NHS-LC-biotinylation kit (Thermo Pierce), according to the manufacturer's instructions. Excess biotin reagent was removed by overnight dialysis in PBS. All streptavidin-coated (SA) biosensors were hydrated in BLI rehydration buffer (PBS, 0.5 mg ml^{-1} BSA and 0.01% (v/v) Tween-20) for 10 minutes. Biotinylated Juno$_{20-228}$ (bait) was diluted in BLI kinetics buffer (PBS, 0.1 mg ml^{-1} BSA and 0.01% (v/v) Tween-20) to a final concentration of 20 μg/ml and immobilized onto a SA-biosensor for 90 seconds. Multiple wild-type or mutant Izumo1$_{22-254}$ (analyte) concentrations were prepared in BLI kinetics buffer and association to Izumo1$_{22-254}$ was measured over 90 seconds at 20°C. Subsequently, the SA-biosensor was immersed into BLI kinetics buffer for 90 seconds to dissociate the analyte. All experiments were performed in triplicate. Two negative controls were performed: BSA and BLI kinetics buffer only against SA-biosensors loaded with biotinylated bait to detect non-specific binding. The data were analyzed and sensorgrams were step corrected, reference corrected and fit globally to a 1:1 binding model. The equilibrium dissociation constant (K_d), association (k_a) and dissociation (k_d) rate constants and its associated standard errors were calculated using the BLItz Pro data analysis (v. 1.1.0.16) software.

Surface plasmon resonance (SPR)

Affinities and kinetics of wild-type Izumo1$_{22-254}$ binding to wild-type Juno$_{20-228}$ were assessed by SPR on a Biosensing Instruments BI-4000 system at 20°C using a CM-dextran sensor chip. Prior to immobilization, pH scouting between pH 4.5–6.5 was performed to identify the optimal pH for immobilization. Wild-type Juno$_{20-228}$ was immobilized using a coupling buffer containing 10 mM sodium acetate pH 5.0 onto one of two flow channels using the manufacturer's standard amine-coupling protocol. Association of the wild-type Izumo1$_{22-254}$ analyte (0.75 μM, 0.5 μM, 0.375 μM, 0.25 μM, 0.188 μM, 0.125 μM, 0.0937 μM and 0 μM) was measured at a flow rate of 50 μl min^{-1} for 90 seconds. The second flow cell, containing no bait, was injected with PBS buffer in a serial flow and used a reference. Subsequently, PBS buffer was injected at a flow rate of 50 μl min^{-1} over 180 seconds to dissociate wild-type Izumo1$_{22-254}$. The cells were regenerated between two analyte runs using the rapid injection protocol involving 8 cycles of 20 μl injections of 0.1 NaOH-acetate pH 9.0 followed by an equal volume of 1X PBS. Measurements were performed in triplicate. The resulting SPR sensorgrams were corrected with the reference and blank (0 μM analyte)

curves, and fitted globally with a 1:1 Langmuir binding model using the BI-Data Analysis and BI-Kinetic Analysis SPR software.

Crystallization and X-ray data collection

Purified Izumo1$_{22-254}$, Izumo1$_{22-268}$, Juno$_{20-228}$, and the Izumo1$_{22-254}$-Juno$_{20-228}$ complex were concentrated to 10 mg ml^{-1}. All crystallization trials were performed at 22°C by sitting drop vapour diffusion (300 nl protein and 300 nl mother liquor) in 96-well low profile Intelliplates (Art Robbins) using an Oryx8 protein crystallization robot (Douglas Instruments).

Izumo1$_{22-254}$ and Izumo1$_{22-268}$

Initial sparse matrix screening of Izumo1$_{22-254}$ and Izumo1$_{22-268}$ constructs identified needle-shaped crystals in multiple conditions. Izumo1$_{22-254}$ and Izumo1$_{22-268}$ crystals were manually optimized in 48-well MRC Maxi crystallization plates using 2 µl sitting drops. Larger needle-shaped Izumo1$_{22-254}$ crystals appeared the next day and reached a maximum length of ~250 µm within 3–4 days in 0.07 M sodium acetate [pH 4.6], 5.6% (w/v) PEG 4000 and 30% (v/v) glycerol. Larger Izumo1$_{22-268}$ crystals were more difficult to obtain and required further optimization using random microseed matrix screening (rMMS) with the Oryx8[31]. rMMS led to thicker needle crystals in 0.085 M HEPES sodium salt [pH 7.5], 8.5% (v/v) isopropanol, 17% (w/v) PEG 4000 and 15% (v/v) glycerol. These crystals reached the final length of ~200 µm within 4–5 days. All crystals were cryoprotected and flash-cooled in liquid nitrogen. Izumo1$_{22-254}$ and Izumo1$_{22-268}$ crystals diffracted to Bragg spacings of 3.1-Å and 2.9-Å, respectively, and datasets were remotely collected at the Canadian Light Source (CLS; Saskatoon, SK) 08ID-1 beamline (Supplementary Fig. 8).

Juno$_{20-228}$

Rod-shaped Juno$_{20-228}$ crystals were grown in 0.02 M magnesium chloride, 0.1 M HEPES sodium salt [pH 7.5], 22% (w/v) Polyacrylic acid 5100. Crystals typically appeared after 3–4 days and reached full-size in 1 week. The mother liquor supplemented with increasing amounts of sucrose (up to 30% (w/v) in final solution) was used as a cryoprotectant before being rapidly cooled in liquid nitrogen. Juno crystals readily produced Bragg reflections better than 2.0-Å resolution on a Rigaku FR-E Superbright X-ray generator and Saturn A200 HD CCD detector (Rigaku Corp.), and a 1.8-Å resolution dataset was collected at the Structural Genomics Consortium X-ray diffraction facility (Toronto, ON, Canada) (Supplementary Fig. 8).

Izumo1$_{22-254}$-Juno$_{20-228}$ complex

Crystals of the protein complex were grown in sitting drops containing equal volumes (1 µl) of purified protein and crystallant (0.1 M MES [pH 6.5], 20% (w/v) PEG 4000 and 0.6 M NaCl). Crystals were observed after 3 days and matured to full-size within a week. Crystals were cryoprotected by sequential soaking in mother liquor with 5%, 10%, 20% and 30% (w/v) sucrose. Crystals were directly immersed into liquid nitrogen and screened at the CLS beamline 08ID-1. A dataset was collected from a single Izumo1$_{22-254}$-Juno$_{20-228}$ complex crystal diffracting to 2.4-Å resolution (Supplementary Fig. 9).

Structure determination and refinement

All diffraction data were integrated and reduced with the XDS program package[32] and scaled using Aimless[33] from the CCP4 program suite. Crystallographic data collection and final refinement statistics are presented in Extended Data Table 1.

$Juno_{20-228}$

The structure of $Juno_{20-228}$ was determined by molecular replacement (MR) with Phaser[34] using the human folate receptor-α (PDB ID: 4LRH) as the search model. Initial characterization of the $Juno_{20-228}$ X-ray data using phenix.xtriage[35] and DETWIN[36] indicated translational pseudosymmetry[37] (TPS) and near-perfect merohedral twinning[38] with an estimated twin fraction of 0.45 (Supplementary Fig. 8). The twinning fraction was calculated from the cumulative distribution of H[39] and Britton plots[40], with the twin fractions related by the twin law k, h, -l. It was necessary to apply the twin law throughout the refinement to further refine the $Juno_{20-228}$ structure using phenix.refine[41].

$Izumo1_{22-254}$-$Juno_{20-228}$ complex

The initial phases for the $Izumo1_{22-254}$-$Juno_{20-228}$ complex were calculated via MR with Phaser[34], using the human folate receptor-α structure (PDB ID: 4LRH) as an initial search model. One clear solution (Z=14.6) was identified. Strong electron density was observed for $Juno_{20-228}$ and the 4HB domain of $Izumo1_{22-254}$. The poly-alanine chain of the $Izumo1_{22-254}$ was initially traced by a combination of phenix.autobuild[42] and manual building with Coot[43].

Validation of proper sequence registry was confirmed by locating the sulphur anomalous signals from methionine and cysteine residues. Multi-crystal sulphur anomalous data were collected on native $Izumo1_{22-254}$-$Juno_{20-228}$ complex crystals. The X-ray beam was focused to 50 μm and the sulphur anomalous signal was measured at a wavelength of 1.7712-Å using a MarMosaic MX300 CCD detector (Rayonix). All crystals were rod-shaped and >400 μm in length, thus allowing us to translate along the rotation axis to expose a fresh undamaged part of the crystal. 360º of data with a rotation angle of 1.0º per frame were collected for each set before translating to a new part of the crystal. Each dataset was processed individually with anomalous signal using XDS[32]. Twenty-four datasets with R_{meas}<10% were merged together using XSCALE[32] and converted to CCP4 data format using XDSCONV[32], F2MTZ and CAD[36]. The overall R_{merge} and anomalous multiplicity for the merged dataset to 2.8-Å resolution were 9.9% and 89.6, respectively. An anomalous difference Fourier electron density map was calculated using PHENIX[35] and confirms the correct location for all 38 protein sulphur sites (Supplementary Fig. 9).

$Izumo1_{22-254}$ and $Izumo1_{22-268}$

The structures of $Izumo1_{22-254}$ and $Izumo1_{22-268}$ were determined by MR. An initial MR search using the refined $Izumo1_{22-254}$ structure from the $Izumo1_{22-254}$-$Juno_{20-228}$ complex failed, likely due to conformational changes between the 4HB and Ig-like domains. A MR search was performed first using the Izumo1 Ig-like domain (residues 167-254) followed by a second MR search using the 4HB and hinge regions (residues 22-166). Clear solutions were identified for both sections in $Izumo1_{22-254}$ and $Izumo1_{22-268}$.

All structures were manually rebuilt using Coot[43] and refined using phenix.refine[41]. No non-crystallographic (NCS) symmetry restraints were employed except in the case of $Juno_{20-228}$, where a 4-fold NCS was applied. All β–strands and α–helices were real-space refined with torsional secondary structural restraints using Coot. Torsion-angle simulated annealing refinement, starting at 5000 K, with individual atomic displacement and Translation/Liberation/Screw (TLS) groups was carried out using Phenix. Due to the lower resolutions of the $Izumo1_{22-254}$ and $Izumo1_{22-268}$ data, these structures were refined with grouped B-factor refinement. Calculation of annealed $2|F_o|–|F_c|$ composite omit maps[44] helped minimize model bias during rebuilding.

Validation and structure analysis

The stereochemical quality of the all refined models was validated using MolProbity[45], PROCHECK[46] and Coot[43]. No residues were identified in disallowed regions of the Ramachandran plot. Moreover, the R values, B-factors, and rmsd bond lengths and angles of all structural models are consistent with other deposited structures determined at similar resolutions, as validated by polygon.phenix[35]. All structural representations were prepared using PyMOL (v. 1.7.4 Schrödinger, LLC.)

Small-angle X-ray scattering (SAXS) data collection and reconstruction

SAXS provides medium-resolution visualization of global structural conformational changes in solution. SAXS experiments were performed by mail-in SAXS on beamline 12.3.1 (SIBYLS) at the Advanced Light Source (Berkeley, CA). Various protein concentrations of tag-cleaved, deglycosylated wild-type and mutant $Izumo1_{22-254}$, $Juno_{20-228}$ and $Izumo1_{22-254}$-$Juno_{20-228}$ complexes, along with matching buffer obtained from SEC (10 mM Tris-HCl [pH 8.0], 150 mM NaCl and 2% (v/v) glycerol), were loaded into a 96-well PCR plate (Axygen) and stored at 4°C prior to data collection. Samples were loaded into the SAXS sample cell using a Hamilton syringe robot. For the wild-type $Izumo1_{22-254}$, $Juno_{20-228}$ and $Izumo1_{22-254}$-$Juno_{20-228}$ complex, data were collected at a wavelength (λ) of 1.0-Å using a MarCCD 165 detector (Rayonix) positioned at a distance of 1.5 m, resulting in scattering vector q of 0.01-$Å^{-1}$ < q < 0.32-$Å^{-1}$ (where $q = 4\pi\sin(\theta/2)/\lambda$ and θ is the scattering angle). Each data set was recorded at 283 K in a succession of three X-ray exposures of 0.5, 1, 2 and 5 seconds. For the mutant $Izumo1_{22-254}$-$Juno_{20-228}$ complexes, data were collected at 1.0-Å wavelength using a Pilatus3X 2M detector (Dectris) (0.01-$Å^{-1}$ <q < 0.55-$Å^{-1}$). Data for the mutant $Izumo1_{22-254}$-$Juno_{20-228}$ complexes were recorded in a time slicing mode of 0.5 second exposures over 15 seconds (30 frames per sample). Data for buffer blanks were collected before each protein image and subsequently buffer subtracted. Sample radiation damage was assessed by overlaying short and long exposures and detecting for any shifts in the scattering curves using the program SCATTER[47]. Concentration and aggregation effects were detected by comparing the lowest scattering angles for each of the protein samples. Fits to the Guinier region were made using autoRg. In order to maximize the signal-to-noise ratio, the SAXS scattering curve at the highest concentration that is free of interparticle interference was used for subsequent analysis. The characteristic real-space distance distribution function, *P(r)*, was determined from the scattering data using an indirect Fourier transformation and the maximum dimension, D_{max}[48]. All *ab initio* reconstructions of molecular envelopes from SAXS data were performed using the program DAMMIN[49].

Twenty-three DAMMIN models were superimposed and averaged by the program DAMAVER[50] to obtain a consensus averaged structure. Alignment of the SAXS reconstructions with the final refined crystal structures was performed using Chimera[51].

Deuterium exchange mass spectrometry (DXMS)

DXMS, which measures kinetics of backbone amide solvent exchange, provides local residue-level conformational dynamics. Prior to performing deuterium exchange experiments, the optimal proteolysis conditions were established as previously described[52,53] to maximize peptide sequence coverage of tag-cleaved, deglycosylated $Izumo1_{22-254}$ and $Juno_{20-228}$. Briefly, 1 μl of diluted protein stock solution (2 mg ml^{-1} in 10mM Tris [pH 7.2], 150mM NaCl) was mixed with 5 μl of quench buffer (6.4 M GuHCl and 1.0 M TCEP in 0.8% (v/v) formic acid, 16.6% (v/v) glycerol). After incubating on ice for various times (2, 5, 10, 15 and 30 min), the quenched samples were mixed with 24 μl of dilution buffer (0.8% (v/v) formic acid, 16.6% (v/v) glycerol) and then subjected to proteolysis and LC-MS analysis. The $Izumo1_{22-254}$-$Juno_{20-228}$ complex was formed by mixing $Izumo1_{22-254}$ and $Juno_{20-228}$ at 1:1.2 or 1.2:1 molar ratios and incubating the samples at 22°C for 2 hours. Deuterium exchange was initiated by mixing 3.5 μl of protein stock solution ($Izumo1_{22-254}$, $Izumo1_{22-254}$-$Juno_{20-228}$, $Juno_{20-228}$ or $Juno_{20-228}$-$Izumo1_{22-254}$) with 7 μl of D_2O buffer (8.3 mM Tris [pH 7.2], 150 mM NaCl in D_2O, pD_{read} 7.2) and incubating at 0°C for 10, 100, 1000, 10,000 and 100,000 seconds. At indicated times, 2.1 μl of exchange samples were added to 10.5 μl quench solution to stop the D_2O exchange reaction. After 5 minutes ($Izumo1_{22-254}$ or $Izumo1_{22-254}$-$Juno_{20-228}$) or 10 minutes ($Juno_{20-228}$ or $Juno_{20-228}$-$Izumo1_{22-254}$) incubation on ice, quenched samples were diluted by addition of 48 μl of ice-cold dilution buffer, and then immediately frozen on dry ice and stored at –80°C. The non-deuterated control samples and equilibrium-deuterated control samples were also prepared by mixing protein with H_2O buffer (8.3 mM Tris [pH 7.2], 150 mM NaCl in H_2O) and equilibrium-deuterated buffer (0.8% (v/v) formic acid in 99.9% D_2O)[54]. The frozen samples were then thawed at 5°C and passed over an immobilized pepsin column (16 μl bed volume) at a flow rate of 20 μl/min. The resulting peptides were collected on a C_{18} trap for desalting and separated by a Magic AQ C_{18} reverse phase column (Michrom BioResources) using a linear gradient of acetonitrile from 6.4% to 38.4% over 30 min. MS analysis was performed using the OrbiTrap Elite Mass Spectrometer (ThermoFisher Scientific), with a capillary temperature of 200°C. Data were acquired in both data-dependent MS/MS mode and MS1 profile mode, and the data were analyzed by Proteome Discoverer software and DXMS Explorer[55] (Sierra Analytics Inc., Modesto, CA).

Extended Data

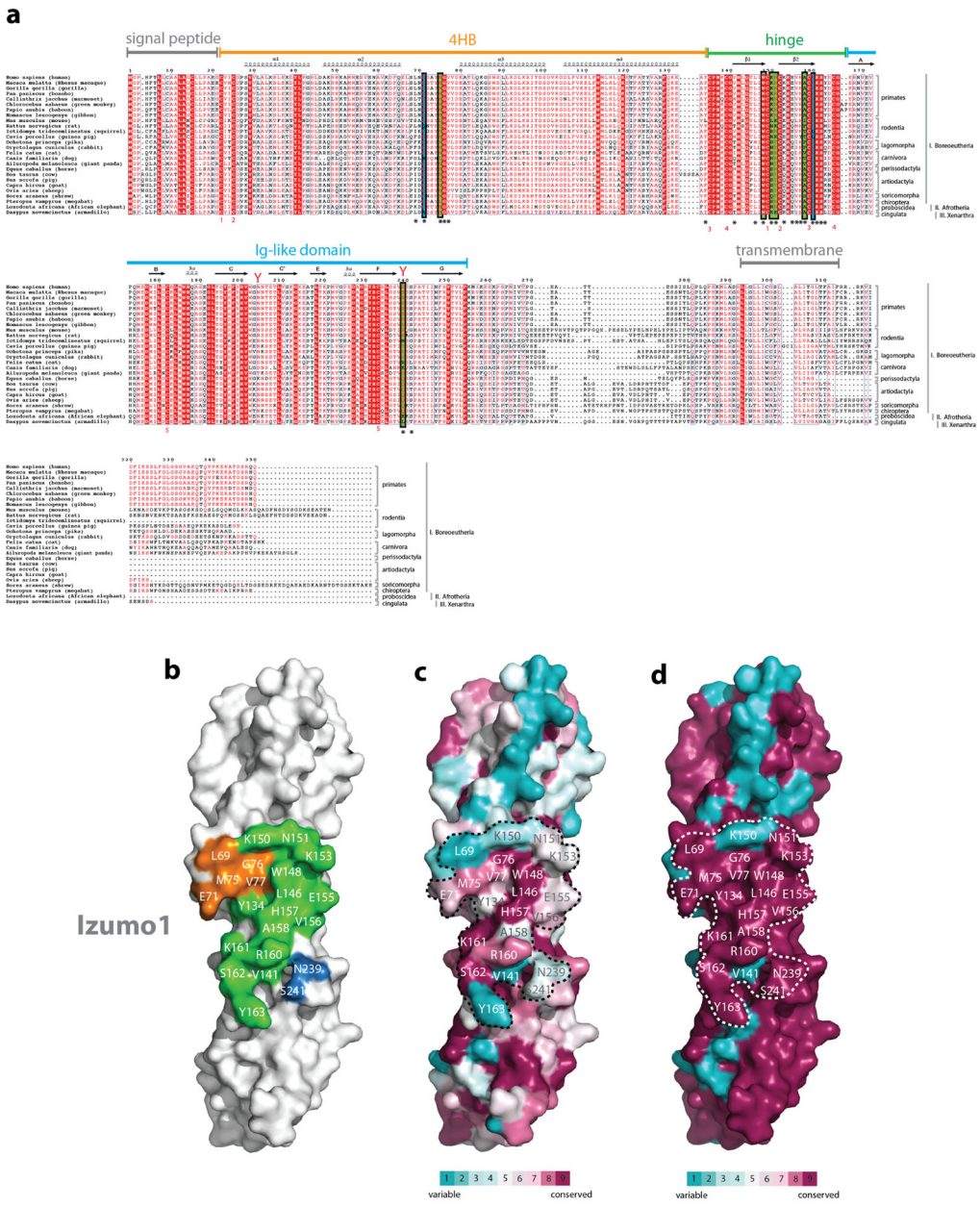

Extended Data Figure 1. Conservation of Izumo1 residues

(a) Alignment of Izumo1 protein sequences from various mammals. Izumo1 sequences from *Homo sapiens* (human; GenBank: BAD91012.1), *Macaca mulatta* (rhesus macaque; GenBank: EHH30233.1), *Gorilla gorilla* (gorilla; Uniprot: G3QFY5), *Pan paniscus* (bonobo; NCBI: XP_003814124.1), *Callinthrix jacchus* (marmoset; Uniprot: F7H859), *Chlorocebus sabaeus* (green monkey; Uniprot: A0A0D9S2Z4), *Papio anubis* (baboon; Uniprot: A0A0A0MU86), *Nomascus leucogenys* (gibbon; Uniprot: G1QXF7), *Mus musculus* (mouse; GenBank: BAD91011.1), *Rattus norvegicus* (rat; GenBank: BAD91013.1), *Ictidomys tridecemlineatus* (squirrel; Uniprot: I3N2L9), *Cavia porcellus* (guinea pig;

Uniprot: H0UTJ7), *Ochotona princeps* (pika; NCBI: XP_004597241.1), *Oryctolagus cuniculus* (rabbit; Uniprot: G1TVX5), *Felis catus* (cat; NCBI: XP_006941089.1), *Canis familiaris* (dog, Uniprot: F6UM65), *Ailuropoda melanoleuca* (giant panda, Uniprot: G1M882), *Equus caballus* (horse; Uniprot: F6YE25), *Bos taurus* (cow; Uniprot: E1BDA8), *Sus scrofa* (pig; Uniprot: F1RIQ7), *Capra hircus* (goat; Uniprot: C6ZEA2), *Ovis aries* (sheep; Uniprot: W5PRD0), *Sorex araneus* (shrew; NCBI: XP_004619786.1), *Pteropus vampyrus* (megabat; NCBI: XP_011372928.1), *Loxodonta africana* (African elephant; NCBI: XP_003406572.1), and *Dasypus novemcinctus* (armadillo; NCBI: XP_004451154.1) are aligned. Red boxes indicate complete conservation of a given amino acid. N-linked glycosylation sequons (N-x-S/T) are indicated by red-coloured Y-shaped symbols. Secondary structural elements observed in the crystal structure of Izumo1 are shown as arrows for β-strands and coils for α-helices. Residues that interact with Juno are identified with asterisks, with those that form salt bridges and hydrogen bonds highlighted in blue and green boxes, respectively. Cysteine pairs involved in disulphide bond formation are numbered in red underneath each sequence. **(b)** Footprint of Juno on the molecular surface of Izumo1. Representation of surface residue conservation, calculated using ConSurf and the alignment of **(c)** all mammalian Izumo1 or **(d)** primate-only Izumo1 sequences from Extended Data Figure 1a. Degree of residue conservation is coloured in a gradient from high (burgundy) to low (cyan) variability.

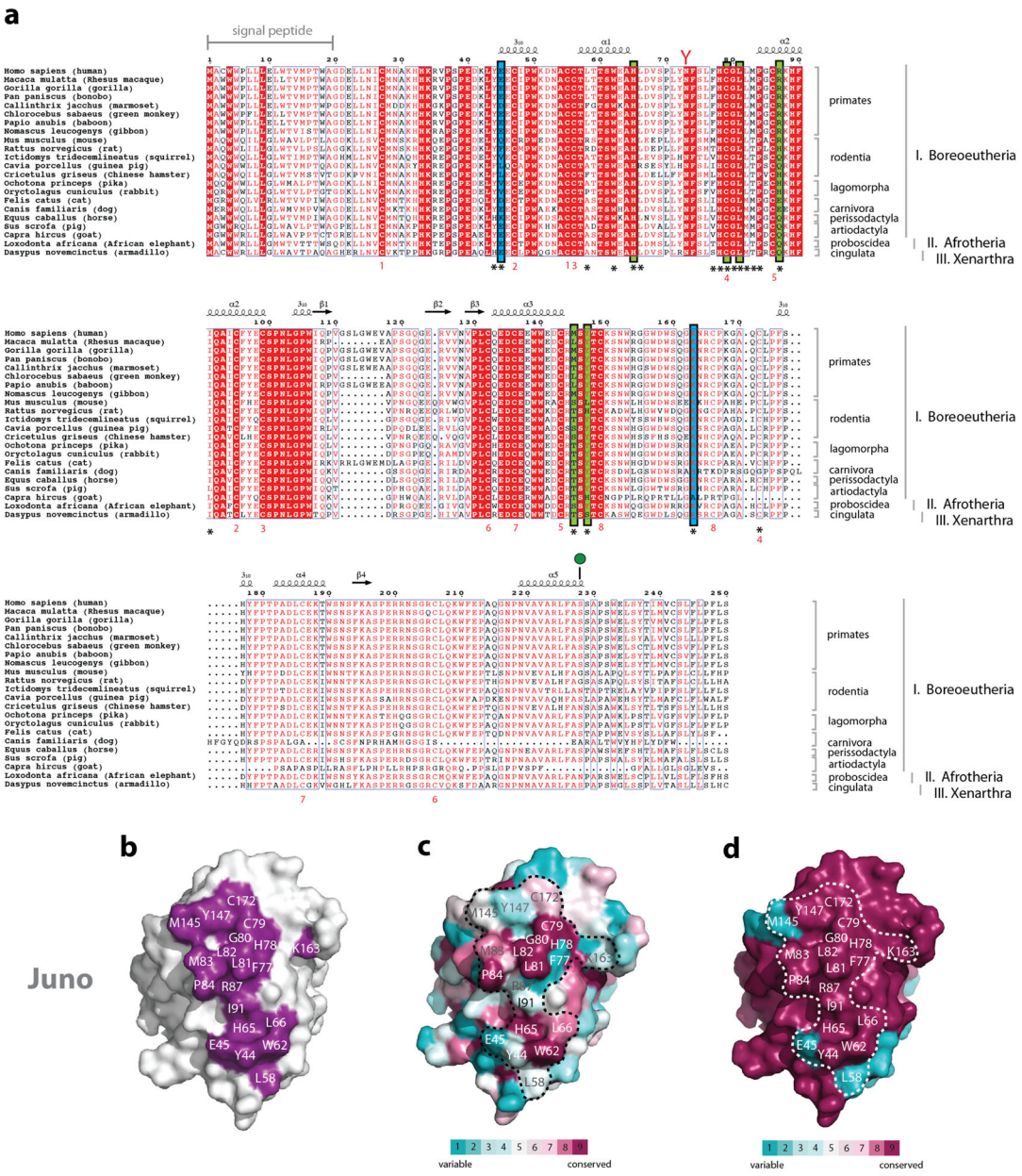

Extended Data Figure 2. Conservation of Juno residues

(a) Alignment of Juno protein sequences from various mammals. Juno/FOLR-δ sequences from *Homo sapiens* (human; NCBI: NP_001186135.1), *Macaca mulatta* (rhesus macaque; NCBI: NP_001180734.1), *Gorilla gorilla* (gorilla; NCBI: XP_004052029.1), *Pan paniscus* (bonobo; NCBI: XP_003813838.1), *Callinthrix jacchus* (marmoset; NCBI: XP_009005477.1), *Chlorocebus sabaeus* (green monkey; Uniprot: A0A0D9S1B0), *Papio anubis* (baboon; NCBI: XP_009185381.1), *Nomascus leucogenys* (gibbon; Uniprot: G1R639), *Mus musculus* (mouse; NCBI: NP_075026.1), *Rattus norvegicus* (rat; NCBI: XP_001072998.2), *Ictidomys tridecemlineatus* (squirrel; NCBI: XP_005337246.1), *Cavia porcellus* (guinea pig; NCBI: XP_003468609.1), *Cricetulus griseus* (Chinese hamster; NCBI: XP_003506544.1) *Ochotona princeps* (pika; NCBI: XP_012782378.1), *Oryctolagus*

cuniculus (rabbit; Uniprot: G1T5D7), *Felis catus* (cat; NCBI: XP_011284828.1), *Canis familiaris* (dog, Uniprot: E2RTK1), *Equus caballus* (horse; NCBI: XP_001491306.1), *Sus scrofa* (pig; Uniprot: F1STK4), *Capra hircus* (goat; NCBI: XP_013824827.1), *Loxodonta africana* (African elephant; NCBI: XP_010593777.1), and *Dasypus novemcinctus* (armadillo; NCBI: XP_004471965.1) are aligned. Red boxes indicate complete conservation of a given amino acid. N-linked glycosylation sequons (N-x-S/T) are indicated by red-coloured Y-shaped symbols. Juno is anchored to the plasma membrane through a GPI anchor at Ser228 (shown as a green lollipop). Secondary structural elements observed in the crystal structure of Juno are shown as arrows for β-strands and coils for α-helices. Residues that interact with Izumo1 are identified with asterisks underneath the sequence, with those that form salt bridges and hydrogen bonds highlighted in blue and green boxes, respectively. Cysteine pairs involved in disulphide bond formation are numbered in red underneath each sequence. **(b)** Footprint of Izumo1 on the molecular surface of Juno. Representation of surface residue conservation, calculated using ConSurf and the alignment of **(b)** all mammalian Juno or **(c)** primate-only Juno sequences from Extended Data Figure 2a. Degree of residue conservation is coloured in a gradient from high (burgundy) to low (cyan) variability.

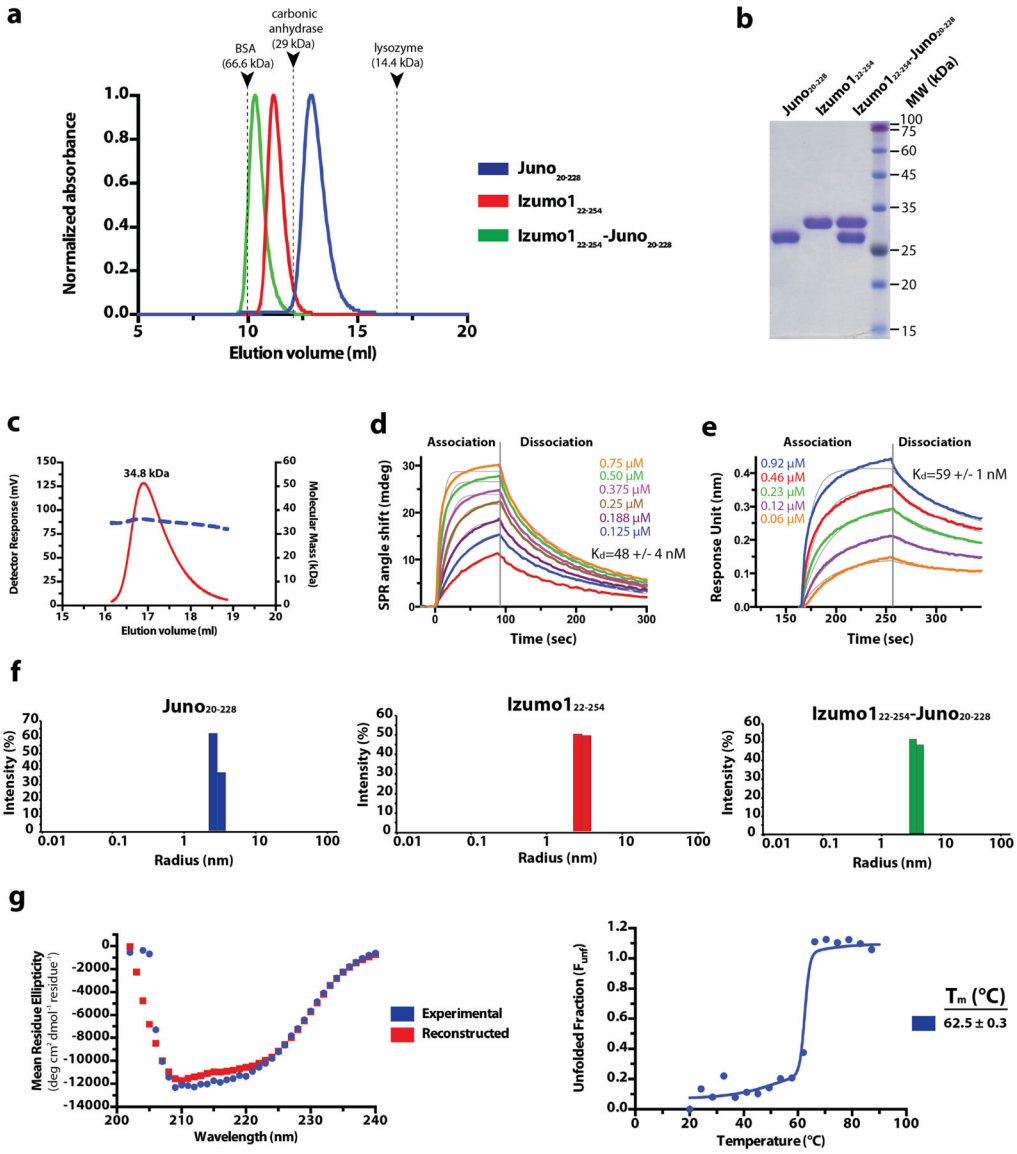

Extended Data Figure 3. Purification and characterization of Izumo1 and Juno

(a) Superdex-75 10/300 GL size-exclusion chromatograms of $Juno_{20-228}$, $Izumo1_{22-254}$, and the $Izumo1_{22-254}$-$Juno_{20-228}$ complex. Eluted peak positions of protein standards are marked with triangles and dashed lines. **(b)** Coomassie-stained SDS-PAGE analysis of the purified $Izumo1_{22-258}$, $Juno_{20-228}$ and $Izumo1_{22-258}$-$Juno_{20-228}$ complex. For gel source data, see Supplementary Figure 1c. **(c)** SEC-MALS profile of glycosylated human $Izumo1_{22-268}$. The detector response unit (mV) and molecular mass (kDa) are plotted against the elution volume from a Superdex-200 Increase 10/300 GL size exclusion column. SEC-MALS reveals an apparent molecular weight (MW) of 34.8 kDa (dashed blue line), which corresponds to a monomeric species. **(d)** Surface plasmon resonance (SPR) binding affinity and kinetic analysis of the human $Izumo1_{22-254}$ and $Juno_{20-228}$ interaction. Human $Juno_{20-228}$ was amine-coupled to the SPR sensor chip. Kinetic parameters were derived from a Langmuir 1:1 binding model. **(e)** Biolayer interferometry (BLI) kinetic analysis of the

human Izumo1$_{22-254}$ and Juno$_{20-228}$ interaction. Human Juno$_{20-228}$ was biotinylated and coupled to streptavidin-coated biosensors. Kinetic parameters were derived from a 1:1 binding model. The experimental curves are shown in colour superimposed with the fitted curves indicated as gray lines. **(f)** A size distribution histogram from dynamic light scattering (DLS) measurements of Izumo1$_{22-254}$, Juno$_{20-228}$ and Izumo1$_{22-254}$-Juno$_{20-228}$ complex at 5 mg ml^{-1}. Izumo1$_{22-254}$, Juno$_{20-228}$, and Izumo1$_{22-254}$-Juno$_{20-228}$ displays a hydrodynamic radii (R_H) of ~3.0 nm, ~2.9 nm, ~3.9 nm, respectively. **(g)** Circular dichroism (CD) wavelength scan of human Izumo1$_{22-268}$ (blue) at 25°C shows mixed secondary structural characteristics. The crystal structure of Izumo1$_{22-268}$ aligns well with the secondary structural content calculated from the CD spectrum (35% α-helical, 24% β-strand, and 41% random coil) from the CD spectra. A reconstructed CD wavelength scan (red) illustrates the agreement of the fit used in secondary structural content analysis. CD thermal denaturation profile of human Izumo1$_{22-268}$ at 222 nm is shown. CD signal was normalized between 0 (folded) and 1 (unfolded), and plotted as a function of temperature. The T_m value indicates the midpoint of the melting transition.

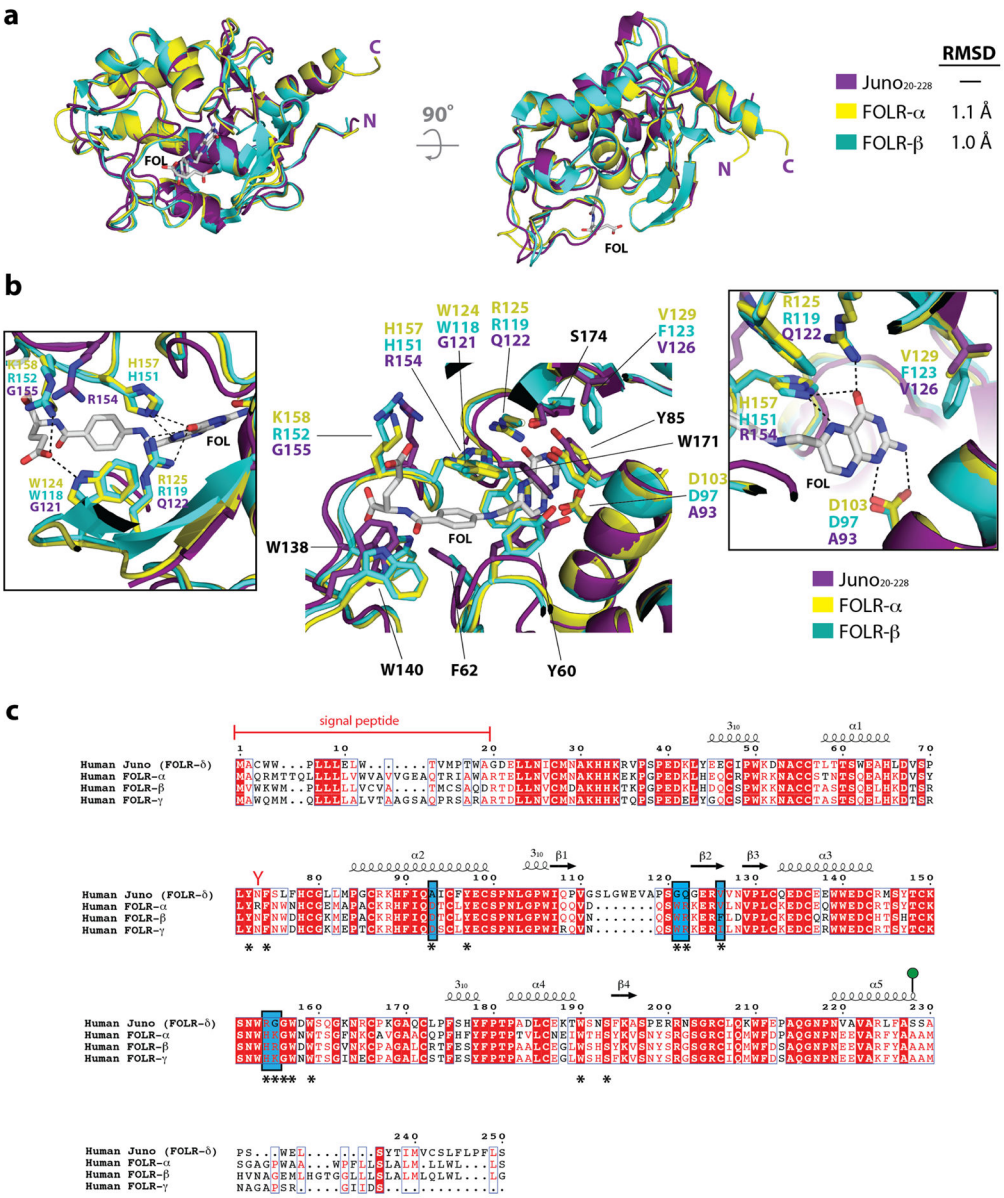

Extended Data Figure 4. Structural comparison of Juno and the folate receptor family of proteins

(a) Structural superimposition of $Juno_{20-228}$ with FOLR-α (PDB ID: 4LRH) and FOLR-β (PDB ID: 4KMZ). Experimentally bound folate (FOL), shown in white sticks, from the FOLR-α structure is positioned in the active site. **(b)** Superimposition of residues in the folate-binding site of human FOLR-α and FOLR-β, and equivalent residues in human Juno. Residue names shown in black are conserved between Juno, FOLR-α, and FOLR-β, and are numbered based on the FOLR-α sequence. Inset boxes highlight the residue differences between Juno, FOLR-α, and FOLR-β. Key hydrogen bond interactions are shown as dashed black lines. Mutagenesis studies showed that replacement of D103/D97, which forms strong interactions to the N1 and N2 nitrogen atoms of the pterin moiety, results in decreased affinity by more than one order of magnitude[15]. Six folate-binding residues observed in

FOLR-α, and FOLR-β (FOLR-α/FOLR-β: D103/D97, W124/W118, R125/R119, V129/F123, H157/H151, and K158/R152) are not conserved in Juno. Four of these residues (FOLR-α/FOLR-β: D103/D97, W124/W118, R125/R119, and H157/H151) form key hydrogen bonds to anchor folate in the active site. In Juno, the substituted residues are not able to maintain the extensive hydrogen bond network seen in FOLR-α and FOLR-β to folate. **(c)** *Homo sapiens* FOLR-α (Uniprot: P15328), FOLR-β (Uniprot: P14207), FOLR-γ (Uniprot: P41439) and FOLR-δ (Uniprot: A6ND01) are aligned. Red boxes indicate complete conservation of a given amino acid. N-linked glycosylation sequons (N-x-S/T) are indicated by red-coloured Y-shaped symbols. Juno is anchored to the plasma membrane through a GPI anchor at Ser228 (shown as a green lollipop). Experimentally determined secondary structural elements are shown as arrows for β-strands and coils for α-helices. Key folate-binding residues, identified from the FOLR-α and FOLR-β crystal structures, are identified with an asterisk underneath the sequence. Key residues difference between Juno, FOLR-α and FOLR-β folate binding sites are highlighted in a blue box.

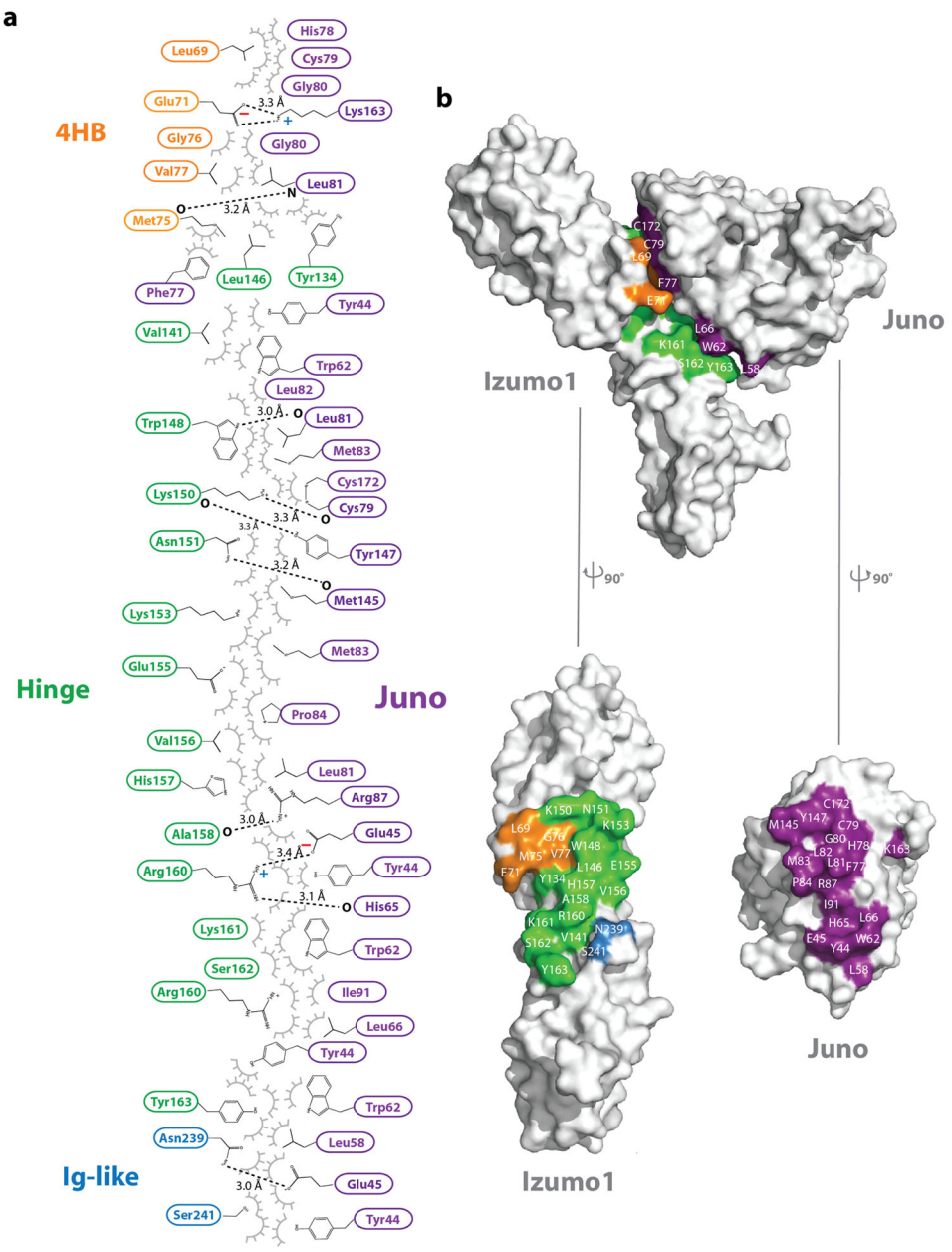

Extended Data Figure 5. Izumo1-Juno interface

(a) 2D schematic of the interactions between Izumo1$_{22-254}$ and Juno$_{20-228}$. Residues from the Izumo1 4HB, hinge, and Ig-like regions, as well as Juno are coloured in orange, green, blue, and purple, respectively. Hydrogen-bond interactions are shown as dashed lines, and van der Waals forces are depicted as grey semi-circles. **(b)** Footprint of Juno on the surface of Izumo1 and Izumo1 on the surface of Juno. The molecular surfaces of Izumo1 and Juno are coloured white with residues forming interactions coloured similarly to panel (a). No N-linked glycans on either Izumo1$_{22-254}$ or Juno$_{20-228}$ are involved in binding. Formation of this interface results in a calculated free energy gain of −10.4 kcal/mol.

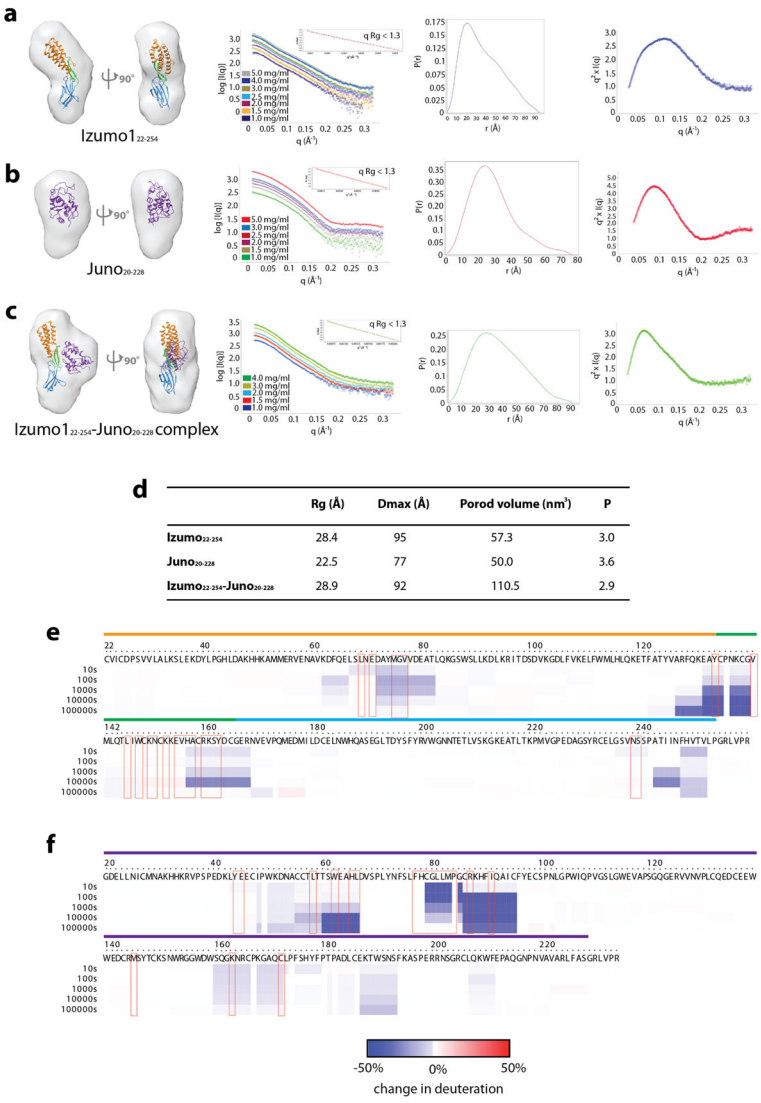

	Rg (Å)	Dmax (Å)	Porod volume (nm^3)	P
Izumo$_{22-254}$	28.4	95	57.3	3.0
Juno$_{20-228}$	22.5	77	50.0	3.6
Izumo$_{22-254}$-Juno$_{20-228}$	28.9	92	110.5	2.9

Extended Data Figure 6. Hybrid structural analysis of human Izumo1 and Juno in a solution state

Ab initio small-angle X-ray scattering (SAXS) reconstruction, experimental scattering curves, normalized pair distance distribution function, *P(r)* and Kratky plot showing the degree of flexibility of **(a)** Izumo1$_{22-254}$, **(b)** Juno$_{20-228}$, and the **(c)** Izumo1$_{22-254}$-Juno$_{20-228}$ complex. No concentration-dependent or radiation effects were observed in the SAXS data. The inset box in the experimental scattering data shows linearity in the Guinier plot at low *q* (*qRg <1.3*). The Izumo1$_{22-254}$, Juno$_{20-228}$ and Izumo1$_{22-254}$-Juno$_{20-228}$ complex crystal structures were docked into the SAXS reconstructed molecular envelopes. The boomerang shape and upright conformation seen in the crystal structures of unbound and bound Izumo1$_{22-254}$, respectively, were recapitulated by the SAXS reconstructions. **(d)** Summary of the experimentally derived SAXS parameters for Izumo1$_{22-254}$, Juno$_{20-228}$ and Izumo1$_{22-254}$-Juno$_{20-228}$. The program SCATTER[47] was used to calculate the radius of gyration (Rg), maximum linear dimension (D_{max}), and to perform Porod-Debye analysis to obtain the Porod volume and P coefficient. Comparative deuterium exchange mass

spectrometry (DXMS) profile of unbound and bound **(e)** Izumo1$_{22-254}$ and **(f)** Juno$_{20-228}$. The plots reveal the change in individual deuterium exchange for all observable residues. The coloured lines above the residue numbers correspond to the observed regions in the crystal structures.

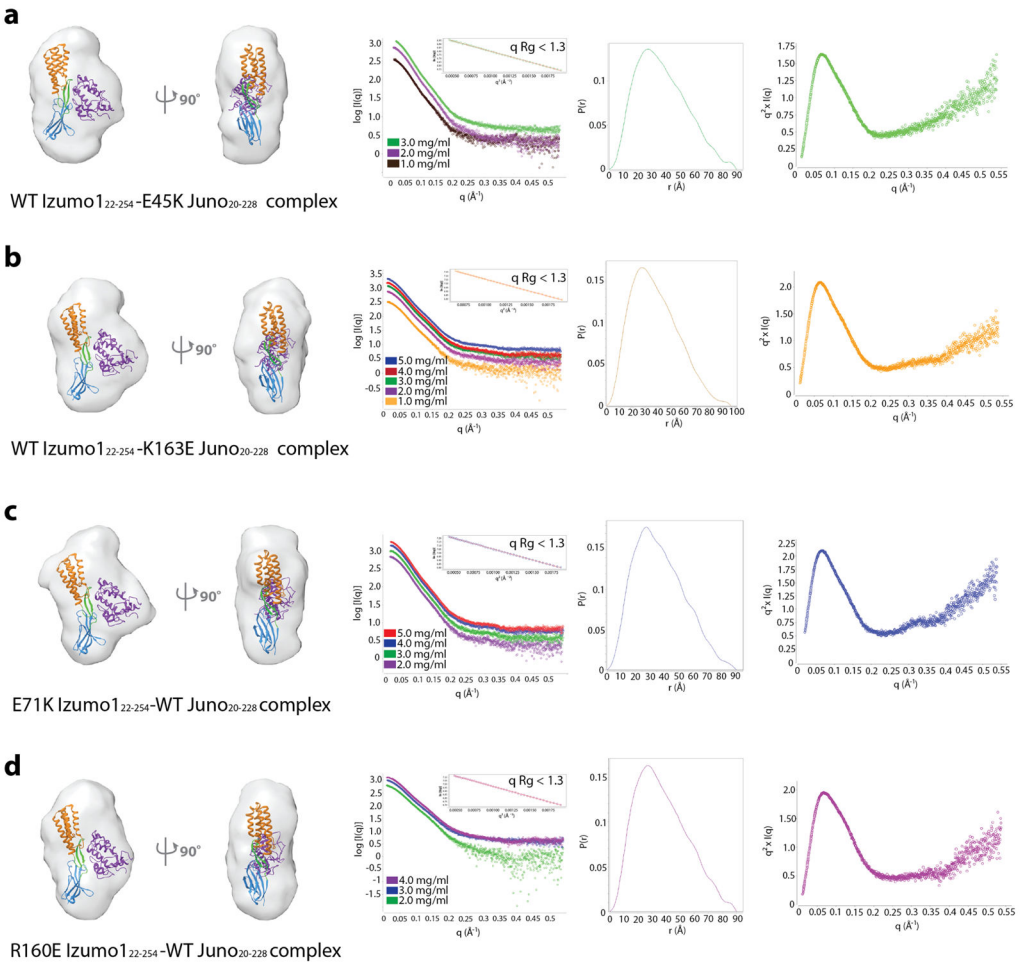

e

	Rg (Å)	Dmax (Å)	Porod volume (nm^3)	P
E71K Izumo$_{22-254}$-WT Juno$_{20-228}$	29.5	91	109.4	2.9
R160E Izumo$_{22-254}$-WT Juno$_{20-228}$	29.5	90	110.7	2.8
WT Izumo$_{22-254}$-E45K Juno$_{20-228}$	29.5	90	110.5	2.8
WT Izumo$_{22-254}$-K163E Juno$_{20-228}$	29.6	97	110.6	3.0

Extended Data Figure 7. SAXS reconstruction of Izumo1 and Juno mutants

(a) *Ab initio* small-angle X-ray scattering (SAXS) reconstruction, experimental scattering curves, normalized pair distance distribution function, *P(r)* and Kratky plot showing the degree of flexibility of **(a)** WT Izumo1$_{22-254}$-E45K Juno$_{20-228}$, **(b)** WT Izumo1$_{22-254}$-K163E Juno$_{20-228}$, **(c)** E71K Izumo1$_{22-254}$-WT Juno$_{20-228}$, and **(d)** R160E Izumo1$_{22-254}$-WT Juno$_{20-228}$ complexes. No concentration-dependent or radiation effects were observed. The inset box shows linearity in the Guinier plot at low *q* (*qRg <1.3*). The WT Izumo1$_{22-254}$-WT Juno$_{20-228}$ complex crystal structure was docked into the SAXS reconstructed molecular

envelopes. **(e)** Summary of the experimentally derived SAXS parameters for the various Izumo1-Juno complexes. The program SCATTER[47] was used to calculate the radius of gyration (Rg), maximum linear dimension (D_{max}), and to perform Porod-Debye analysis to obtain the Porod volume and P coefficient.

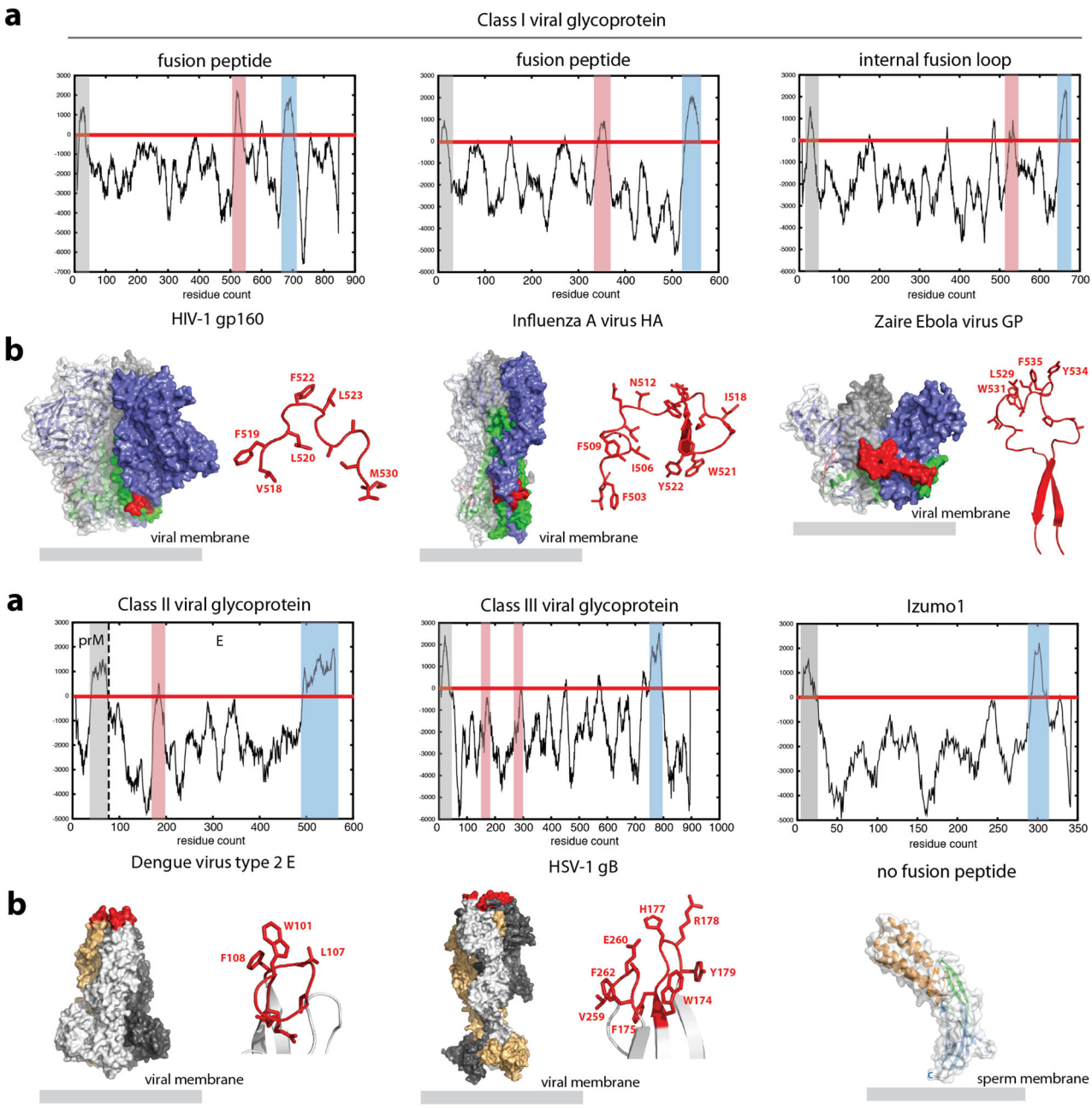

Extended Data Figure 8. Comparison of Izumo1 with selected viral fusogens

A common feature of many viral fusogens is the presence of a hydrophobic fusion peptide or fusion loop. **(a)** A Kyte and Doolittle hydropathy plot was calculated for Izumo1, HIV-1 gp160, influenza A HA, Ebola virus GP, Dengue virus type 2 E, and herpes simplex virus-1

gB to detect the presence of hydrophobic regions. Class I and class II viral fusion glycoproteins (GPs) contain three clear hydrophobic regions corresponding to the signal peptide (highlighted in grey), fusion peptide or loop (highlighted in red) and the transmembrane anchor (highlighted in blue). For class III viral GPs, the presence of a signal peptide and transmembrane anchor are clear, however the hydrophobic fusion loop is formed by two discontinuous regions. This results in a lower hydropathy scale that is more difficult to detect. Two regions of hydrophobic residues cluster at the tip of the GP (shown in red) and are thought to be the internal fusion loop. In all class I, II and III viral fusion GPs, a clustering of aromatic and hydrophobic residues in a loop or helical region are hallmark features of the proteins for fusion. In contrast, Izumo1 clearly does not have any hydrophobic regions or structural features similar to the viral fusogens that could insert into the egg membrane. **(b)** Molecular surface representation of the class I, II, and III viral GPs and Izumo1. The fusion peptide/loop is shown as red sticks and also coloured red on the GP surface. For the class I viral GPs, the metastable prefusion trimer is shown, with the receptor binding and fusion subunits shown in blue and green, respectively. For the class II and class III viral GPs, the postfusion trimer is shown with three hydrophobic fusion loops clustered at the tip of the molecule.

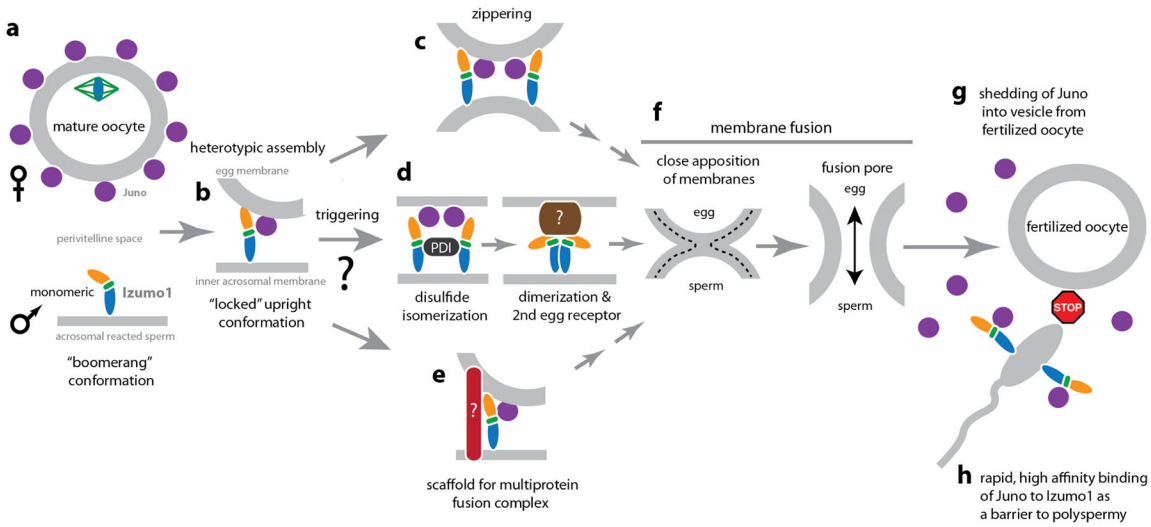

Extended Data Figure 9. Model of Izumo1 and Juno in sperm-egg fertilization

During fertilization, mature sperm undergoes an acrosome reaction and penetrates through the egg zona pellucida to reach the perivitelline space. The acrosome reaction also causes relocalization of Izumo1 to the sperm equatorial segment. **(a)** Izumo1 adopts a monomeric boomerang conformation on the surface of the sperm membrane. **(b)** Upon binding to the Juno egg receptor, Izumo1 undergoes a conformational change. The 4HB region migrates towards the egg membrane. Moreover, the hinge region of Izumo1 becomes more rigid and "locks" the molecule into an upright position. The formation of the Izumo1 and Juno complex provides a direct physical link between the egg and sperm membranes. It is currently not clear whether Izumo1 requires a post-Juno binding event to trigger the fusion process, however, at least three potential mechanisms are possible. **(c)** The heterotypic assembly of Izumo1 and Juno, or a secondary conformational change in Izumo1, may bring

the egg and sperm membranes into close proximity for fusion to take place. **(d)** Inoue *et al.* proposed that subsequent to Izumo1-Juno binding, a protein disulphide isomerase (PDI) catalyzes a thio-disulphide exchange reaction that leads to structural conformation change and dimerization of Izumo1[26]. The Izumo1 dimer releases Juno and contacts a yet to be discovered oocyte receptor that facilitates membrane fusion. **(e)** Alternatively, Izumo1 may act as a scaffold to recruit other sperm or egg protein partners to form a multiprotein fusion complex in a manner similar to some viral fusogens. **(f)** The mergers of the egg and sperm membranes will require the apposition of the two bilayers to initiate initial mixing of the outer membrane leaflets and formation of a hemifusion stalk. The hemifused bilayers open to form the full fusion pore. **(g)** Following fusion, Juno is rapidly shed into extracellular vesicles from the fertilized oocyte. Within 30–40 minutes, Juno is weakly or barely detectable on the membrane surface of zona-intact or anaphase II-stage zona-free fertilized oocytes, and undetectable at the pronuclear stage[6]. **(h)** Izumo1 binds Juno tightly and rapidly (BLI: K_d = 59 +/− 1 nM, k_a= 1.15 × 10^5 M^{-1} s^{-1}; SPR: 48 +/− 4 nM, k_a=4.2 × 10^5 M^{-1} s^{-1}), and once shed, Juno is able to bind to exposed Izumo1 on incoming acrosomal-reacted sperm in the perivitelline space to act as a “sperm-sink” to block polyspermy.

Extended Data Table 1

Izumo1-Juno binding interface mutations

Technique	Protein	Role of residue	K_d	k_a (× 10^5) (M s)$^{-1}$	k_d (× 10^{-3}) (s)$^{-1}$
SPR	Wild-type	n/a	48 +/− 4 nM	4.2 +/− 0.2	19.4 +/− 0.9
BLI	Wild-type	n/a	59 +/− 1 nM	1.15 +/− 0.02	6.7 +/− 0.1
Izumo1 mutants					
BLI	E71A Izumo1$_{22-254}$	salt bridge with Juno K163; L2 leash	96 +/− 13 nM	1.43 +/− 0.04	13.7 +/− 0.2
BLI	E71K Izumo1$_{22-254}$	salt bridge with Juno K163; L2 leash	119 +/− 19 nM	1.65 +/− 0.04	19.5 +/− 0.3
BLI	D72A Izumo1$_{22-254}$	H-bond to Q130 in unbound state	71 +/− 8 nM	1.78 +/− 0.04	12.6 +/− 0.2
BLI	Q130A Izumo1$_{22-254}$	H-bond to D72 in unbound state	56 +/− 19 nM	1.27 +/− 0.03	6.8 +/− 0.1
BLI	W148A Izumo1$_{22-254}$	conserved interface residue	*no binding detected*		
BLI	H157A Izumo1$_{22-254}$	conserved interface residue	1.8 +/− 1 μM	0.51 +/− 0.05	79 +/− 2
BLI	R160A Izumo1$_{22-254}$	salt bridge with Juno E45	730 +/− 78 nM	0.78 +/− 0.04	56.3 +/− 0.9
BLI	R160E Izumo1$_{22-254}$	salt bridge with Juno E45	2.2 +/− 1.2 μM	0.32 +/− 0.02	51.2 +/− 1.1
Juno mutants					
BLI	E45A Juno$_{20-228}$	salt bridge with Izumo1 R160	681 +/− 141 nM	0.37 +/− 0.01	24.7 +/− 0.5
BLI	E45K Juno$_{20-228}$	salt bridge with Izumo1 R160	2.8 +/− 0.2 μM	0.23 +/− 0.02	62.4 +/− 1.7

Technique	Protein	Role of residue	K_d	k_a ($\times 10^5$) ($M\ s)^{-1}$	k_d ($\times 10^{-3}$) $(s)^{-1}$
BLI	W62A $Juno_{20-228}$	conserved interface residue	361 +/− 24 nM	1.14 +/− 0.04	41.2 +/− 0.6
BLI	L81A $Juno_{20-228}$	conserved interface residue	9.1 +/− 0.4 μM	0.4 +/− 0.3	349 +/− 23
BLI	K163A $Juno_{20-228}$	salt bridge with Izumo1 E71	97 +/− 9 nM	1.38 +/− 0.03	13.3 +/− 0.2
BLI	K163E $Juno_{20-228}$	salt bridge with Izumo1 E71	134 +/− 4 nM	1.81 +/− 0.05	24.2 +/− 0.3

* kinetic and binding affinity values are presented as the mean of technical triplicates (n=3) and errors as the standard deviation of the mean

K_d- dissociation constant

k_a - rate of association

k_a - rate of dissociation

Supplementary Material

Refer to Web version on PubMed Central for supplementary material.

Acknowledgments

This work was supported by a CIHR Operating Grant (MOP-115066), NSERC Discovery Grant (RGPIN 435607-13), Ontario Early Researcher Award (ER-13-09-116), and a Canada Research Chair to J.E.L. S.L. is supported by grants from NIH (1U19AI117905, R01 GM020501 and R01 AI101436). Moreover, support for stipends were provided by University of Toronto and Ontario Graduate Scholarships to H.A., and a NSERC USRA to A.T.. The authors would like to thank Drs. Walid Houry and Trevor Moraes in the Department of Biochemistry (University of Toronto), and Christopher Spring at St. Michael's Hospital (Toronto) for access to their CD, SEC-MALS and SPR systems, respectively. This work is based upon X-ray data collected at beamline 08ID-1 at the Canadian Light Source (CLS; Saskatoon, SK) and Structural Genomics Consortium (SGC), and SAXS data acquired at the Advanced Light Source (ALS) SIBYLS beamline 12.3.1. CLS is supported by NSERC, National Research Council of Canada, CIHR, the Province of Saskatchewan, Western Economic Diversification Canada, and the University of Saskatchewan. ALS (Berkeley, CA) is a national user facility operated by Lawrence Berkeley National Laboratory on behalf of the Department of Energy (Office of Basic Energy Sciences) through the Integrated Diffraction Analysis Technologies program (DE-AC02-05CH11231), supported by DOE Office of Biological and Environmental Research; additional support comes from NIH project MINOS (R01GM105404). The authors would like to thank Farshad Azimi, Jonathan Cook, Aiping Dong (SGC) and Dr. Nguyen Ly (Biosensing Instruments) for technical support, and Drs. Erica Ollmann Saphire, Anthony S. Rocca and George Bikopoulos for critical reading of the manuscript.

References

1. Wassarman PM, Jovine L, Litscher ES. A profile of fertilization in mammals. Nat Cell Biol. 2001; 3:E59–E64. [PubMed: 11175768]
2. Evans JP. Sperm-Egg Interaction. Annu Rev Physiol. 2012; 74:477–502. [PubMed: 22054237]
3. Sutovsky P. Sperm–egg adhesion and fusion in mammals. Expert Rev Mol Med. 2009; 11
4. Klinovska K, Sebkova N, Dvorakova-Hortova K. Sperm-Egg Fusion: A Molecular Enigma of Mammalian Reproduction. Int J Mol Sci. 2014; 15:10652–10668. [PubMed: 24933635]
5. Inoue N, Ikawa M, Isotani A, Okabe M. The immunoglobulin superfamily protein Izumo is required for sperm to fuse with eggs. Nature. 2005; 434:234–238. [PubMed: 15759005]
6. Bianchi E, Doe B, Goulding D, Wright GJ. Juno is the egg Izumo receptor and is essential for mammalian fertilization. Nature. 2014; 508:483–487. [PubMed: 24739963]
7. Ellerman DA, et al. Izumo is part of a multiprotein family whose members form large complexes on mammalian sperm. Mol Reprod Dev. 2009; 76:1188–1199. [PubMed: 19658160]

8. Yanagimachi R. Fertility of mammalian spermatozoa: its development and relativity. Zygote. 1994; 2:371–372. [PubMed: 8665172]
9. Gupta SK, et al. Mammalian zona pellucida glycoproteins: structure and function during fertilization. Cell Tissue Res. 2012; 349:665–678. [PubMed: 22298023]
10. Kim E, et al. Sperm penetration through cumulus mass and zona pellucida. Int J Dev Biol. 2008; 52:677–682. [PubMed: 18649281]
11. Grayson P, Civetta A, Grayson P, Civetta A. Positive Selection and the Evolution of izumo Genes in Mammals, Positive Selection and the Evolution of izumo Genes in Mammals. Int J Evol Biol. 2012:e958164.
12. Marquardt T, Helenius A. Misfolding and aggregation of newly synthesized proteins in the endoplasmic reticulum. J Cell Biol. 1992; 117:505–513. [PubMed: 1315315]
13. Halaby DM, Poupon A, Mornon JP. The immunoglobulin fold family: sequence analysis and 3D structure comparisons. Protein Eng. 1999; 12:563–571. [PubMed: 10436082]
14. Wibowo AS, et al. Structures of human folate receptors reveal biological trafficking states and diversity in folate and antifolate recognition. Proc Natl Acad Sci. 2013; 110:15180–15188. [PubMed: 23934049]
15. Chen C, et al. Structural basis for molecular recognition of folic acid by folate receptors. Nature. 2013; 500:486–489. [PubMed: 23851396]
16. Han L, et al. Divergent evolution of vitamin B9 binding underlies Juno-mediated adhesion of mammalian gametes. Curr Biol. 2016; 26:R100–R101. [PubMed: 26859261]
17. Inoue N, et al. Molecular dissection of IZUMO1, a sperm protein essential for sperm-egg fusion. Development. 2013; 140:3221–3229. [PubMed: 23824580]
18. Ohto U, et al. The crystal structure of the IZUMO1-JUNO complex reveals an essential step for sperm-oocyte recognition during mammalian fertilization. Nature. 2016 advance online publication.
19. Monné M, Han L, Schwend T, Burendahl S, Jovine L. Crystal structure of the ZP-N domain of ZP3 reveals the core fold of animal egg coats. Nature. 2008; 456:653–657. [PubMed: 19052627]
20. Han L, et al. Insights into Egg Coat Assembly and Egg-Sperm Interaction from the X-Ray Structure of Full-Length ZP3. Cell. 2010; 143:404–415. [PubMed: 20970175]
21. Chen EH, Olson EN. Unveiling the Mechanisms of Cell-Cell Fusion. Science. 2005; 308:369–373. [PubMed: 15831748]
22. Wilson IA, Skehel JJ, Wiley DC. Structure of the haemagglutinin membrane glycoprotein of influenza virus at 3 A resolution. Nature. 1981; 289:366–373. [PubMed: 7464906]
23. Pérez-Vargas J, et al. Structural Basis of Eukaryotic Cell-Cell Fusion. Cell. 2014; 157:407–419. [PubMed: 24725407]
24. Subramanian RP, Geraghty RJ. Herpes simplex virus type 1 mediates fusion through a hemifusion intermediate by sequential activity of glycoproteins D, H, L, and B. Proc Natl Acad Sci. 2007; 104:2903–2908. [PubMed: 17299053]
25. Sathiyamoorthy K, et al. Assembly and Architecture of the EBV B Cell Entry Triggering Complex. PLoS Pathog. 2014; 10:e1004309. [PubMed: 25144748]
26. Inoue N, Hagihara Y, Wright D, Suzuki T, Wada I. Oocyte-triggered dimerization of sperm IZUMO1 promotes sperm-egg fusion in mice. Nat Commun. 2015; 6:8858. [PubMed: 26568141]
27. Mohan GS, Li W, Ye L, Compans RW, Yang C. Antigenic Subversion: A Novel Mechanism of Host Immune Evasion by Ebola Virus. PLoS Pathog. 2012; 8:e1003065. [PubMed: 23271969]
28. Dolnik O, et al. Ectodomain shedding of the glycoprotein GP of Ebola virus. EMBO J. 2004; 23:2175–2184. [PubMed: 15103332]
29. Whitmore L, Wallace BA. DICHROWEB, an online server for protein secondary structure analyses from circular dichroism spectroscopic data. Nucleic Acids Res. 2004; 32:W668–W673. [PubMed: 15215473]
30. Sultana A, Lee JE. Measuring protein-protein and protein-nucleic acid interactions by biolayer interferometry. Current Protocols in Protein Science. 2015; 79:19.25.1–26.
31. D'Arcy A, Villard F, Marsh M. An automated microseed matrix-screening method for protein crystallization. Acta Crystallogr D Biol Crystallogr. 2007; 63:550–554. [PubMed: 17372361]

32. Kabsch W. XDS. Acta Crystallogr D Biol Crystallogr. 2010; 66:125–132. [PubMed: 20124692]
33. Evans PR, Murshudov GN. How good are my data and what is the resolution? Acta Crystallogr D Biol Crystallogr. 2013; 69:1204–1214. [PubMed: 23793146]
34. McCoy AJ, et al. *Phaser* crystallographic software. J Appl Crystallogr. 2007; 40:658–674. [PubMed: 19461840]
35. Adams PD, et al. *PHENIX* : a comprehensive Python-based system for macromolecular structure solution. Acta Crystallogr D Biol Crystallogr. 2010; 66:213–221. [PubMed: 20124702]
36. Potterton E, Briggs P, Turkenburg M, Dodson E. A graphical user interface to the *CCP* 4 program suite. Acta Crystallogr D Biol Crystallogr. 2003; 59:1131–1137. [PubMed: 12832755]
37. Zwart PH, Grosse-Kunstleve RW, Lebedev AA, Murshudov GN, Adams PD. Surprises and pitfalls arising from (pseudo)symmetry. Acta Crystallogr D Biol Crystallogr. 2008; 64:99–107. [PubMed: 18094473]
38. Dauter Z. Twinned crystals and anomalous phasing. Acta Crystallogr D Biol Crystallogr. 2003; 59:2004–2016. [PubMed: 14573956]
39. Yeates TO. Simple statistics for intensity data from twinned specimens. Acta Crystallogr A. 1988; 44:142–144. [PubMed: 3272147]
40. Fisher RG, Sweet RM. Treatment of diffraction data from crystals twinned by merohedry. Acta Crystallogr Sect A. 1980; 36:755–760.
41. Afonine PV, et al. Towards automated crystallographic structure refinement with *phenix. refine*. Acta Crystallogr D Biol Crystallogr. 2012; 68:352–367. [PubMed: 22505256]
42. Terwilliger TC, et al. Iterative model building, structure refinement and density modification with the *PHENIX AutoBuild* wizard. Acta Crystallogr D Biol Crystallogr. 2008; 64:61–69. [PubMed: 18094468]
43. Emsley P, Lohkamp B, Scott WG, Cowtan K. Features and development of *Coot*. Acta Crystallogr D Biol Crystallogr. 2010; 66:486–501. [PubMed: 20383002]
44. Terwilliger TC, et al. Iterative-build OMIT maps: map improvement by iterative model building and refinement without model bias. Acta Crystallogr D Biol Crystallogr. 2008; 64:515–524. [PubMed: 18453687]
45. Chen VB, et al. *MolProbity* : all-atom structure validation for macromolecular crystallography. Acta Crystallogr D Biol Crystallogr. 2010; 66:12–21. [PubMed: 20057044]
46. Laskowski RA, MacArthur MW, Moss DS, Thornton JM. PROCHECK: a program to check the stereochemical quality of protein structures. J Appl Crystallogr. 1993; 26:283–291.
47. Förster S, Apostol L, Bras W. *Scatter* : software for the analysis of nano- and mesoscale small-angle scattering. J Appl Crystallogr. 2010; 43:639–646.
48. Rambo RP, Tainer JA. Accurate assessment of mass, models and resolution by small-angle scattering. Nature. 2013; 496:477–481. [PubMed: 23619693]
49. Svergun DI. Restoring Low Resolution Structure of Biological Macromolecules from Solution Scattering Using Simulated Annealing. Biophys J. 1999; 76:2879–2886. [PubMed: 10354416]
50. Volkov VV, Svergun DI. Uniqueness of *ab initio* shape determination in small-angle scattering. J Appl Crystallogr. 2003; 36:860–864.
51. Pettersen EF, et al. UCSF Chimera—A visualization system for exploratory research and analysis. J Comput Chem. 2004; 25:1605–1612. [PubMed: 15264254]
52. Marsh JJ, et al. Structural Insights into Fibrinogen Dynamics Using Amide Hydrogen/Deuterium Exchange Mass Spectrometry. Biochemistry. 2013; 52:5491–5502. [PubMed: 23875785]
53. Sheerin DJ, et al. Inter- and intra-molecular interactions of Arabidopsis thaliana DELLA protein RGL1. Biochem J. 2011; 435:629–639. [PubMed: 21323638]
54. Li S, et al. Mechanism of Intracellular cAMP Sensor Epac2 Activation cAMP-Induced Conformational Changes Identified by Amide Hydrogen/Deuterium Exchange Mass Spectrometry (DXMS). J Biol Chem. 2011; 286:17889–17897. [PubMed: 21454623]
55. Zhang Z, Smith DL. Determination of amide hydrogen exchange by mass spectrometry: A new tool for protein structure elucidation. Protein Sci. 1993; 2:522–531. [PubMed: 8390883]

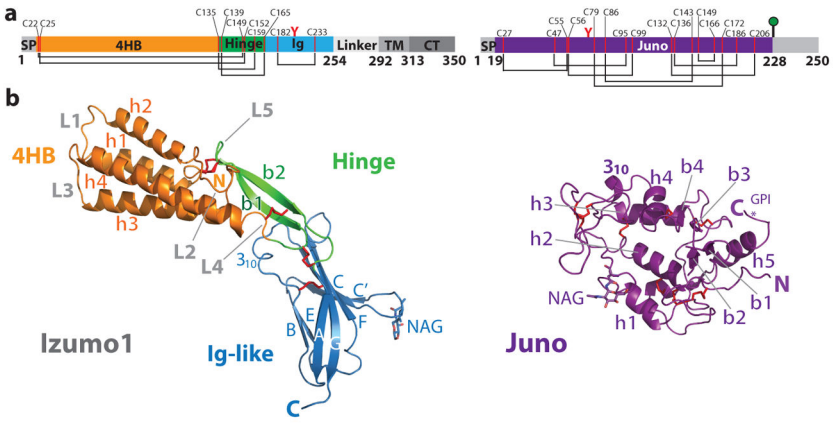

Figure 1. Overall structure of human Izumo1 and Juno

(a) Domain schematic of human Izumo1 and Juno. Red Y-shaped and green lollipop symbols denote N-linked glycans and a glycophosphatidylinositol (GPI)-anchor, respectively. Regions not observed in the crystal structure are shaded grey. Abbreviations: SP, signal peptide; 4HB, four-helix bundle; Hinge; Ig, immunoglobulin-like domain; TM, transmembrane region; CT, cytoplasmic tail. **(b)** Ribbon representation of unbound $Izumo1_{22-254}$ and $Juno_{20-228}$. Cysteine residues that form conserved disulphide linkages are highlighted in red.

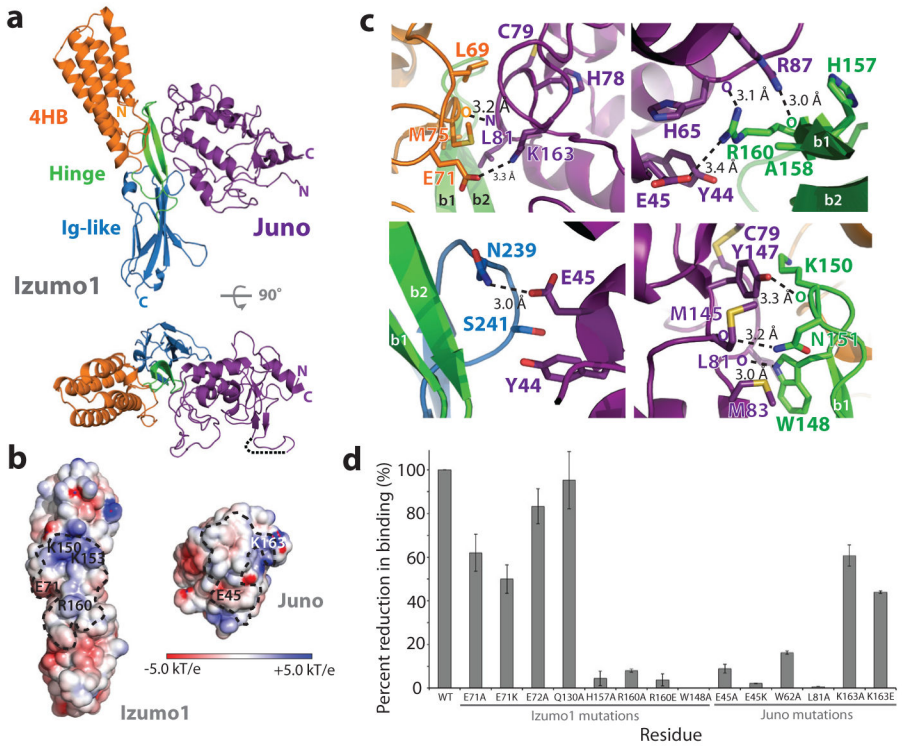

Figure 2. Izumo1-Juno heterotypic assembly

(a) Crystal structure of the human Izumo1$_{22-254}$-Juno$_{20-228}$ complex shown as a ribbon diagram. Izumo1$_{22-254}$ and Juno$_{20-228}$ are coloured according to Figure 1. A disordered loop between the β1 and β2 strands of the Juno$_{20-228}$ is shown with a black dashed line. **(b)** Electrostatic potential surface representation of the Izumo1$_{22-254}$-Juno$_{20-228}$ binding interface. The footprints of the binding interface are shown by black dashed lines. R160 and E71 on Izumo1 form a salt bridge with E45 and K163 on Juno, respectively. **(c)** Binding site interactions of Izumo1$_{22-254}$ and Juno$_{20-228}$. Side chains of key residues involved in hydrogen bond or salt bridge interactions are shown. **(d)** BLI binding affinity analysis of Izumo1$_{22-254}$ and Juno$_{20-228}$ interface mutants. Wild-type Izumo1-Juno interaction is normalized at 100% and the binding affinities (K_d) for each mutant is shown as a percent reduction to wild-type. All experiments were performed with technical triplicates (n=3), with mean K_d values and its standard deviations of the mean presented in Extended Data Table 1.

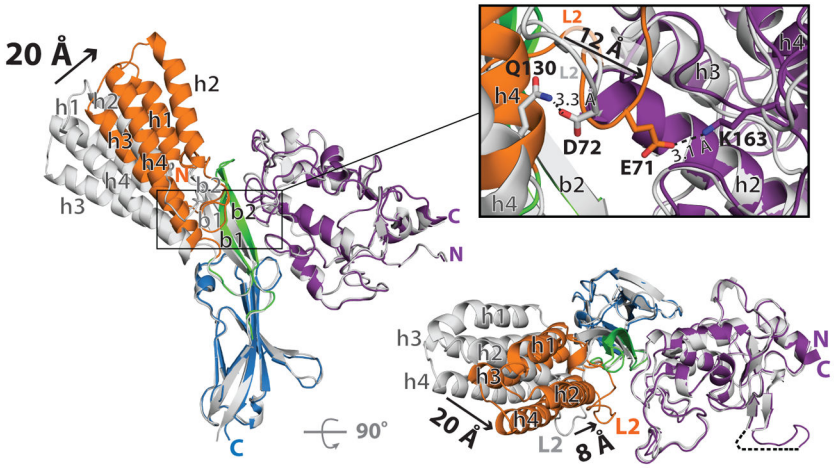

Figure 3. Conformational changes in Izumo1 upon binding to Juno

Superimposition of structures of unbound Izumo1$_{22-254}$ and Juno$_{20-228}$ (shown in grey) on the Izumo1$_{22-254}$-Juno$_{20-228}$ complex (coloured according to Figure 1). Black arrows highlight the positional changes in secondary structure with the corresponding distances shown in Ångstroms. The inset panel displays the conformational changes within the L2 region during formation of the complex. The L2 region residue D72 and α4 helix residue Q130 (both shown in grey) form a hydrogen bond in the unbound Izumo1$_{22-254}$ structure. Upon binding to Juno$_{20-228}$, the L2 region E71 (orange) forms an electrostatic interaction with Juno$_{20-228}$ K163 (purple).

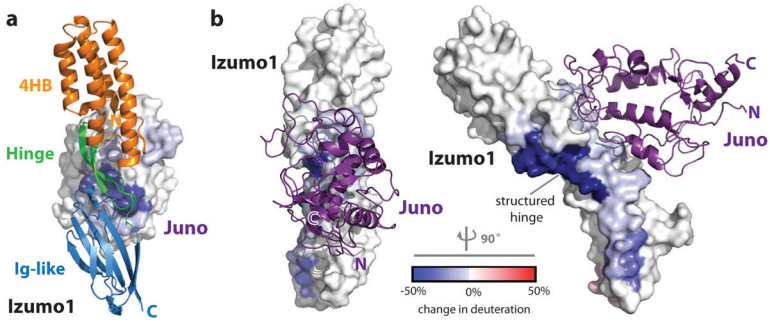

Figure 4. Comparative DXMS profiles of human Izumo1 and Juno binding

Difference of HD exchange upon complex formation is mapped onto the molecular surfaces of **(a)** $Juno_{20-228}$ and **(b)** $Izumo1_{22-254}$.